2011

Application of Active Magnetic Force Actuator for Control of Flexible Rotor System Vibrations

Volodymyr Mykhaylyshyn
Cleveland State University

APPLICATION OF ACTIVE MAGNETIC FORCE ACTUATOR FOR CONTROL OF FLEXIBLE ROTOR SYSTEM VIBRATIONS

VOLODYMYR MYKHAYLYSHYN

Master of Science in

Mechanical Engineering

Ternopil Ivan Pul'uj National Technical University

June, 2001

submitted in partial fulfillment of requirements for the degree

MASTER OF SCIENCE

IN MECHANICAL ENGINEERING

at the

CLEVELAND STATE UNIVERSITY

October, 2011

This thesis has been approved

for the Department of MECHANICAL ENGINEERING

and the College of Graduate Studies by

Dr. Jerzy T. Sawicki, Thesis Committee Chairperson
Department of Mechanical Engineering, CSU

Dr. Stephen F. Duffy
Department of Civil and Environmental Engineering, CSU

Dr. Taysir H. Nayfeh
Department of Mechanical Engineering, CSU

ACKNOWLEDGMENT

I would like to express my heartfelt gratitude to Dr. Jerzy T. Sawicki for his patient understanding, goodness, and guidance through my graduate career. By teaching me to do things right, he changed me and my life. Without his constant support, helpful discussions, and motivation during my education, this thesis would not have been possible.

I would like to thank Dr. Taysir H. Nayfeh and Dr. Stephen F. Duffy, who served on the thesis committee for their consideration, time, and evaluation.

Also I appreciate my lab mate Alexander Pesch for his encouragement and time we spent discussing different problems.

I am grateful to my family for believing in me and support through years of my education.

APPLICATION OF ACTIVE MAGNETIC FORCE ACTUATOR FOR CONTROL OF FLEXIBLE ROTOR SYSTEM VIBRATIONS

VOLODYMYR MYKHAYLYSHYN

ABSTRACT

The purpose of this work was to develop and experimentally demonstrate a novel approach to minimize lateral vibrations of flexible rotor. The applied feed forward control approach employed magnetic force actuator to inject a specially designed force to counteract the rotor unbalance force. By specific selection of frequency and phase as functions of the rotor running speed and rotor natural frequency, the proposed simplified injection waveform has been shown to be effective both in reducing the rotor's vibrations and for hardware implementation. A model of the test rig was constructed using the finite element (FE) method and was validated using experimental data. The effectiveness of the proposed current injection was numerically simulated with FE model and experimentally validated using a residual unbalance force. It was noticed that at a selected constant running speed, just below the first rotor critical speed, the rotor vibrations were reduced approximately by 90%. The method was also implemented during the speed ramp test, which passes through the first critical speed. In this test the proposed force injection also reduced vibrations at various rotor speeds. These results agree well with the results of simulation.

TABLE OF CONTENTS

LIST OF TABLES

Table

LIST OF FIGURES

Figure

NOMENCLATURE

ω	angular velocity
M	mass of the disk
J	polar moment of inertia with respect to the axis of rotation
m	center of mass (heavy spot)
l	distance between center of mass and geometrical center of the disk (eccentricity)
r	radius of the shaft
O	geometrical center of the disk
O_0	position of the geometrical center of the disk without rotation
O_1	position of the geometrical center of the disk at “slow roll”
O_2	position of the geometrical center of the disk at subcritical speed
α	angular position of the center of mass measured from the reference angle zero
β	angular position of the high beat point measured from the reference angle zero
φ	angel between center of mass and respond spot (phase)
φ_0	angel between center of mass and respond spot (phase) at “slow roll”
φ_2	angel between center of mass and respond spot (phase) at subcritical speed
φ_3	angel between center of mass and respond spot (phase) at post critical speed
F	unbalance (exciting) force
F_a	attractive magnetic force
F_1	attractive magnetic force at the location of the center of mass

F_2 attractive magnetic force at the location of the high spot

ε geometric correction factor

μ_0 permeability of free space

A_g single pole face area

N total number of wire coils in a horseshoe

I current in the coil

g air gap distance between rotor and stator

g_{static} nominal air gap distance between rotor and stator

g_1 air gap distance between rotor and stator at the location of the center of mass

g_0 air gap distance between rotor and stator at “slow roll”

g_2 air gap distance between rotor and stator at subcritical speed

g_3 air gap distance between rotor and stator at post critical speed

CHAPTER I

INTRODUCTION

1.1 Background and Motivation.

The dynamic of rotating systems was well understood long time ago thanks to number of mathematicians and theoretical mechanics. Beginning with the ancient world we can observe that scientist showed interest in harmonic motion and vibration. Pythagoreans determined the natural frequency of vibrating system and proved that it is a property of the system in the V century B.C. and Aristotle (384 – 322 B.C.) developed a fundamental understanding of statics and dynamics. Also, archeologists discovered that ancient Chinese scientists invented seismograph, which was used to measure earthquakes.

The modern day theory was probably founded by scientists and mathematicians such Sir Isaac Newton (1642–1737), who gave us calculus and the laws of motion for analyzing vibration; Daniel Bernoulli (1700 – 1782) and Leonard Euler (1707 – 1783) who studied beam vibrations (Bernoulli – Euler beam); and Josef Fourier (1768 – 1830),

who developed the theory of frequency analysis of signals. The technological revolution expanded our present engineering development toward higher speeds and heavier loads on machines, involving higher dynamic stresses caused by increased mechanical vibrations. Proper design and control are crucial in maintaining high performance level and production efficiency, and prolonging the useful life of machinery, structures and industrial processes. The reliability of machines with rotating parts is closely connected with the vibrational characteristic of the rotor as a whole and of its elements and with the maintenance of the permissible level of vibrational stress. Rotordynamic dates from the second half of the nineteenth century. The first systematic work was written by Lord Rayleigh [24] where he introduced a correction to the lateral vibration of the beam due to rotor inertia. Timoshenko [29] presented a model that takes into account shear deformation and rotational inertia effects. Whirling of shafts was investigated by W.A. Rankine [22], who anticipated that shaft operation above critical speed is impossible. The first successful rotor model was proposed by Föppl in 1895. He described a single disk centrally located on a circular shaft, without damping and demonstrated that supercritical operation was stable [8]. Significant work was done by De Laval. His analysis was inaccurately credited to Jeffcott who published his similar work in a widely read English journal [11]. Later the Soviet scientists Nikolai [20] examined the stability of the shaft with a disk mounted in the centre, and the stability of a shaft with the disk attached to the free end. P.L. Kapitsa pointed out that a flexible shaft could become unstable due to friction condition in its sliding bearings [12]. Many rotordynamics textbooks were created, for example, by J.M. Vance [29], Erwin Kramer “Dynamics of Rotors and Foundations” [15], K. Czolczynski [3] discussed aspects affecting the stability of the

system, “Handbook of Rotordynamic” by Frederic F Ehrich [6] reflect devices and phenomena which have entered the practice of rotordynamics engineering. A. Muszynska [18] at her “Fundamental Response of a Rotor” discussed rotor response to the inertia force due to unbalance. J.T. Sawicki [25] at “Unbalance Response Prediction for Accelerating Rotors with Load-Dependent Nonlinear Bearing Stiffness” discussed unbalance response for an accelerating rotor supported on ball bearings. Many other great scientists made their contributions in the study of dynamics of rotating machinery.

The new chapter in these investigations began with the appearance of magnetic actuators, which allow unique application of rotating machinery with excellent performance. Magnetic actuator is typical mechatronics product; it is composed of mechanical and electronic elements. The properties and principles of work will be described in Chapter III. The study of magnetic levitation goes back to S. Earnshaw [5]. Earnshaw’s theorem contends that if inverse square law forces control a flow of charged particles, they can never be stable. The theorem is based on the Laplace partial differential equation. The solution of this equation does not have any local maxima or minima, so there can be no equilibrium. This theorem confirms that it is impossible to have a completely stable system using only forces of static fields of permanent magnets.

The next level of investigation of properties of magnetic actuators was begun in the early forties of the nineteenth century when early magnetic bearing patents were assigned to Jesse Beam. This technology matured with the work of H. Habermann [10] and G. Schweitzer [26], where they developed modern computer-based control technology. A great number of scientists made their contributions to the science of vibration control.

Many different methods and techniques were proposed. Some of them, which are of interest of this work, will be introduced.

1.2 State-of-the-Art of Active Control of Rotor Vibration.

A major problem faced by rotating machinery is the imbalance induced vibration. The flexible rotor may have a variety of unbalance distribution. According to F. Ehrich [6] there are four basic types of unbalance distribution encountered with multimass rotor. First, continuous unbalance distribution along the shaft. The second distribution includes radial unbalances, such as encountered by assembled compressor turbine stages on a shaft. The third distribution represents a shaft with bow. In a bowed rotor the principal axis of inertia (centerline) of the rotor is not concurrent with its axis of rotation. Bows may be introduced by no uniform shrink fits, thermal effects, and permanent sag due to gravitational effects. Fourth is the disk skew. Usually, not only one type of unbalance appears.

There are great number of methods that can be applied to compensate this unbalance [30]. Generally, they can be divided into two main categories: passive and active. In the passive method we ‘assign’ balancing weights and select proper operational speed. Balancing can be done by different methods such as single-plane balancing by influence coefficient method, two-plane balancing by the influence coefficient method, single-plane balancing using static and dynamic components, single-plane balancing by the influence coefficient method using linear regression, generalized influence coefficient method using pseudo-inversion, multiplane balancing using linear programming

techniques, modal balancing, three-trial-weight method of balancing, multiplane balancing without phase, rotor balancing without trial weights, coupling trim balancing and other [6]. All of the methods can be divided into two categories: modal methods and influence coefficient methods. The modal method, based on a rotating structure model, determines experimentally the disturbing unbalance associated with a specific mode. The influence coefficient method uses experimental models that represent the machine's sensitivity to unbalances. Some of them are very interesting but others are expensive and time-consuming. The conditions where these methods can be effective are limited and even though the rotor amplitude may be reduced to small vibrations at the particular location and speed, other points along the rotor may exhibit higher vibrations. At other speeds the rotor may appear not be in balance.

Active methods for vibration control in rotors involve controlled force delivered by actuators. There are different types of actuators such as hydraulic, pneumatic, piezoelectric, and electromagnetic. The advantage of electromagnetic actuators will be described later. Considerable research has already been done on design and application of magnetic actuators [6].

Kari Tammi [28] created a control system for active vibration control of rotor on similar, to presented in this thesis, test environments. He designed controllers using feedback and feedforward control algorithm. This control system determines the force required and applies the force commands to the force control system. The control system design was based on knowledge available about the system to be controlled, and the parameters were assumed invariant in time. However, the higher peaks were observed at post critical rotational speed. The clear explanation for this behavior was not presented.

The study confirms that reductions in rotor's response can be achieved by compensating the disturbance by means of the reference signal.

M.E.F. Kasarda [13] proposed active control solution utilizing active magnetic bearing (AMB) technology in conjunction with conventional support bearings. The AMB is utilized as an active magnetic damper (AMD) at rotor locations inboard of conventional support bearings. Another active magnetic actuator was used as a source of sub synchronous vibration. The study shows that sub synchronous vibrations are reducible with an AMD. The study also shows that the AMD can significantly increase synchronous vibration response (up to 218%) by increasing system stiffness. The overall results from this work demonstrate that full rotor dynamic analysis and design are critical for successful application of this approach.

J.M. Krodkiewski at the University of Melbourne used active hydrodynamic bearing as a third bearing to add damping to the system. A multivariable adaptive self tuning regulator was used to control oil film thickness in the third bearing located between the load carrying ball bearings. The system was designed to cope with non-linear fluid-film bearing characteristics, parameter vibrations and parameter uncertainty. [16].

Interesting results were shown in "Active Balancing of Turbo machinery: Application to Large Shaft Lines" by C. Alauze [1]. The unbalance correction was carried out in real time, during operation in steady state and transient responses. The concept consists of generating a correction force by using two mobile weights situated in the same plane and running at a constant radius of the rotation axis. The balancing process is based on the influence coefficient method and includes specific measurement and control developments. The behavior (Bode plot) of the heavy 5.56m long, 110 to 360 mm

diameter and disk with mass 4.3 tons that situated in the middle was very similar to the behavior of the test rig used at present work.

An interesting method was established by C.R. Knospe [14]. The stability and performance robustness of an adaptive open loop control algorithm was examined. Expressions were derived for a number of unstructured uncertainties. The experimental results indicate that the theoretical expressions do provide an upper bound on actual performance however, this bound is not tight.

Robust modal control design of a magnetically suspended rotor was presented in a simulation study by Hsiang-Chieh Yu [31], involving the finite element formulation. The original system is augmented using the direct output control in the first level, which removes the repeated rigid body modes of an uncontrolled system. In the second level design, a robust controller is implemented in the complex modal space. It has been theoretically shown that the presented control design is robust, but not proved experimentally.

M.S. De Querioz [22] presents the active feedback method that asymptotically learns the unbalance-induced disturbance forces and identifying the unknown unbalance-related parameters of a rotor.

A new approach was proposed by Kai-Yew Lum [17] that differs from the usual adaptive feed-forward compensation. Under the proposed control law, a rigid rotor achieves rotation about the mass center and principal axis of inertia. The calculation and simulation example was done for a rotor supported by two AMBs.

Another good experiment in a similar test environment was done by C.R. Burrows [2] at the University of Bath. In their work “Design and Application of a Magnetic Bearing

for Vibration Control and Stabilization of a Flexible Rotor" they described using a magnetic actuator, control algorithm that determines the amplitude and phase required for each axis and some typical optimum control forces obtained experimentally.

Various active control techniques, applicable to rotating machinery where, presented in work, performed by Heinz Ulbrich [29]. In his "Elements of Active Vibration Control for Rotating Machinery", he presented several topics such as the availability of an appropriate actuator, modeling of the entire system, positioning of actuators and sensors, control concepts that should be used, controllability and observability. Real applications were presented as examples.

1.3 Scope of Work

This work is concerned with the subject of vibrations, system dynamics, magnetic actuators and their combinations. To reduce vibrations of the rotor focus was on synchronous response due to unbalance. Unbalance is one of the most common malfunction of rotating machines; analysis of rotor synchronous response allows to balance the rotor; to understand more complex rotor dynamic behavior caused by various other malfunctions, knowledge of rotor unbalance response is necessary. In order to reduce vibrations, the design of magnetic force actuator was completed (Chapter III) and experimentally verified.

In Chapter II, review of flexible rotor system is presented concerning to application of active magnetic actuator. Also, finite element model of the rotor and methods of solution were described.

A description of the , as well as unique features of active magnetic force actuators and its modifications will be presented in Chapter III.

Unbalance compensation experimental results for sub and super-critical speeds with model identification and force injection are shown in Chapter IV.

Chapter V provides conclusions as well as contributions and a short summary of future research directions.

CHAPTER II

FLEXIBLE ROTOR SYSTEM

2.1 Introduction

"Everything should be made as simple as possible, but not simpler."- Albert Einstein. The Jeffcott rotor has a flexible mass shaft, one rigid disk at the midspan and simple supports as bearings. The Jeffcott rotor model is obviously an over-simplification of real-world rotors but, it helps to understand many features of real-world rotor behavior, including critical speeds, response to unbalance, or the effect of damping.

2.2 Model of Jeffcott rotor

Consider the case of a long and lightweight shaft, rotating with an angular velocity ω and carrying at its midspan a disk of mass M and mass polar moment of inertia with respect to the axis of rotation J. As discussed in the previous chapter, a real flexible rotor may have a variety of unbalance distributions. So, it is assumed that this is just a point mass or heavy spot m on the disc. This unbalance heavy spot m is located at some distance l from the geometrical center of the disc O. This distance l is the disc

eccentricity. To determine the position of m one also needs its angular position α, measured from the reference angle zero, marked on the shaft. Unbalance force F can be characterized by its harmonic time base, expressed by the harmonic functions $\sin(\omega t)$, $\cos(\omega t)$ or $e^{j\omega t} = \cos(\omega t) + j\sin(\omega t)$ (where t is time, ω is angular frequency equal to the rotative speed) and the force amplitude equal $ml\omega^2$. The harmonic unbalance force causes the rotor to respond harmonically.

The equations of motion, with present unbalance force, take the following format:

$$\begin{aligned} M\ddot{x} + D\dot{x} + Kx &= F\cos(\omega t - \alpha) \\ M\ddot{y} + D\dot{y} + Ky &= F\sin(\omega t - \alpha) \end{aligned} \tag{2.1}$$

Where $M\ddot{x}, M\ddot{y}$ represent inertia forces in two orthogonal lateral directions, $D\dot{x}, D\dot{y}$ - damping forces, Kx, Ky - stiffness and F - exciting force (in our case it is unbalance force). In order to cancel the rotor vibrations we need to cancel the exciting force.

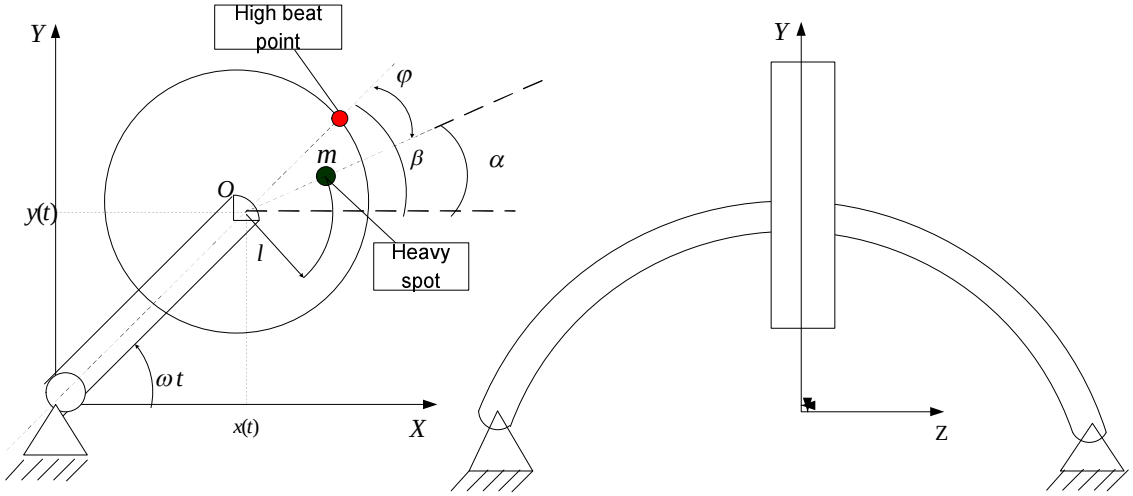

Figure 2.1 Physical model of the rotor.

Cancellation of the exciting force is possible by applying the same harmonic force but in opposite direction. As an instrument to do this an active magnetic actuator (AMA) was chosen.

An active magnetic actuator is a mechatronic device that uses electromagnetic fields to apply forces to a rotor without contact. The advantages of using active magnetic actuators are already well known. Their very low friction, virtually limitless life, insensitivity to surrounding environment and relatively large changes in temperature, and flexibility due to digital computer control, gives them extraordinary versatility. The effectiveness of the active magnetic actuators is based on the nature phenomena of attractive forces that are generated by magnets. See Figure 2.2. for schematic of rotor and magnetic force actuator.

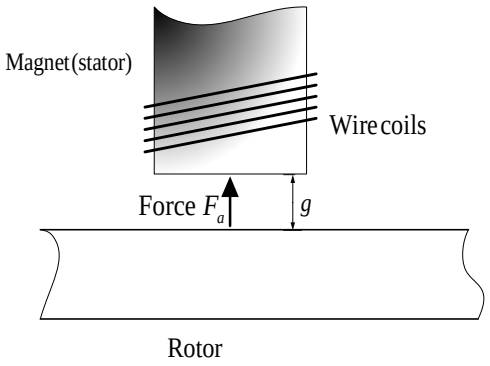

Figure 2.2 Electromagnet (stator) and rotor.

The attractive magnetic force, F_a ,applied to the rotor is determined by the formula:

$$F_a = \frac{\varepsilon \mu_0 A_g N^2 I^2}{4g^2} \tag{2.1}$$

where ε is a geometric correction factor, μ_0 is the permeability of the air gap, A_g is a single pole face area, N is the total number of wire coils in a horseshoe, I is the current in the coil and g is the air gap distance. Now let us see what will happen if the rotor begins to rotate. Figure 2.3 below shows the cross section of an active magnetic actuator with four poles. In the figure, the rotor is shown displaced vertically from the center.

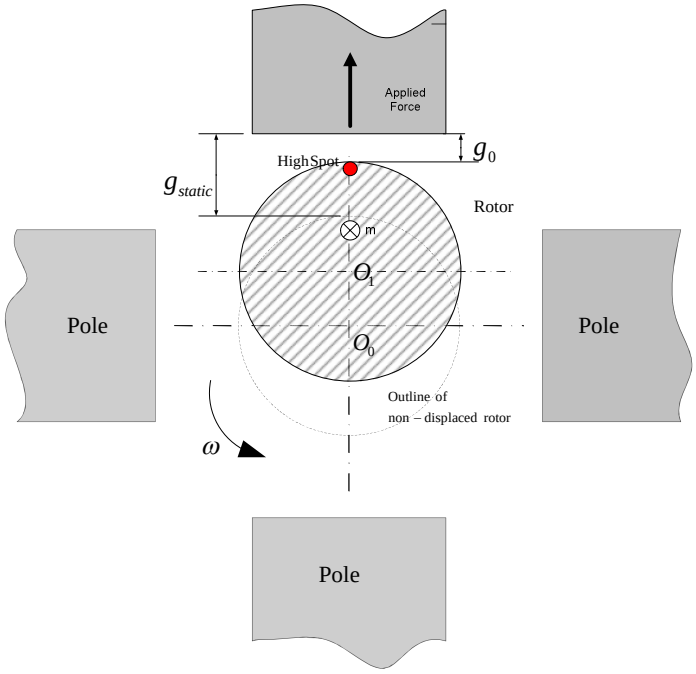

Figure 2.3 Position of the rotor at the slow roll.

At the "slow roll" speed the deflection of the rotor will differ from the static position. Due to an unbalance force, the rotor will have some whirling orbit. The radius of this orbit is the distance between static position of the center of the rotor O_0 and new position

of the geometrical center of the rotor O, plus the radius of the rotor. The position of the center of mass (heavy spot) and response point (high spot) is on the same radial line (Figure 2.3). There is no angle between them, $\varphi_0 \approx 0$.

On the Bode plot, shown in Figure 2.4, this position can be seen on the left side of the graph (low speed).

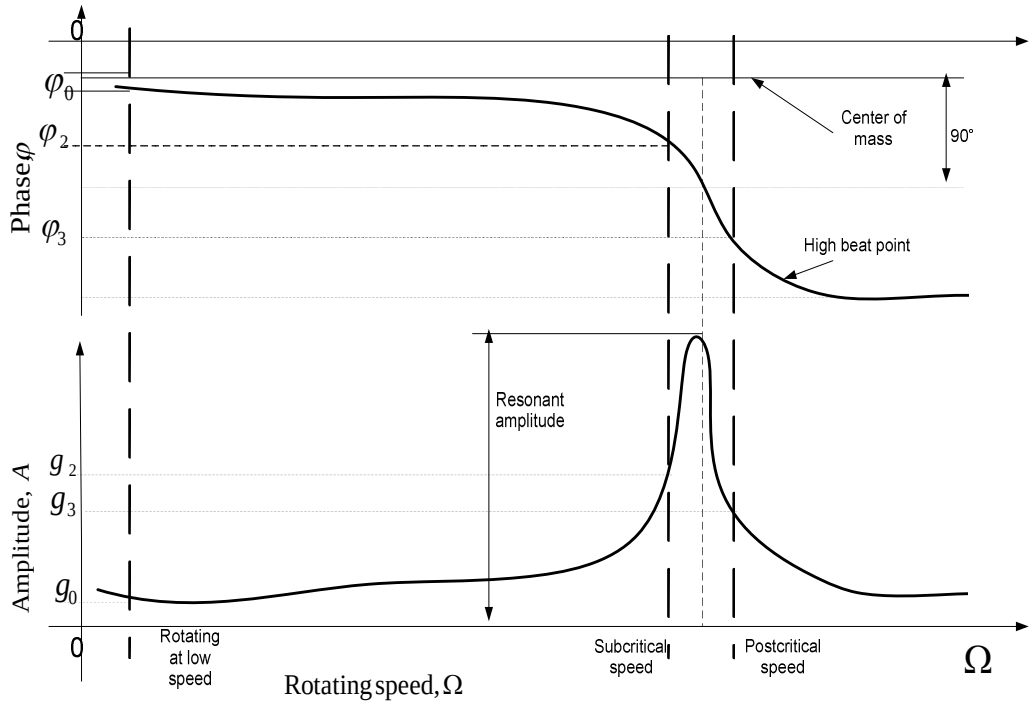

Figure 2.4 Bode plot of the rotor.

On the schematic Bode plot, the line that shows the position of the heavy spot has a fixed location on the rotor. The line of the response spot (or high spot) shows that it increases with the increased rotating speed. Also, the magnitude of vibration of the geometrical center of the rotor grows as resonance is approached. So, to cancel the

unbalance force, one needs to apply an opposite force in the radial direction of the location of the center of mass. At a slow roll, this is also the location of the response (high beat point). The time base plot of the high beat point, center of mass, and unbalance force at a slow roll will be sinusoidal waves and are all in phase (Figure 2.5).

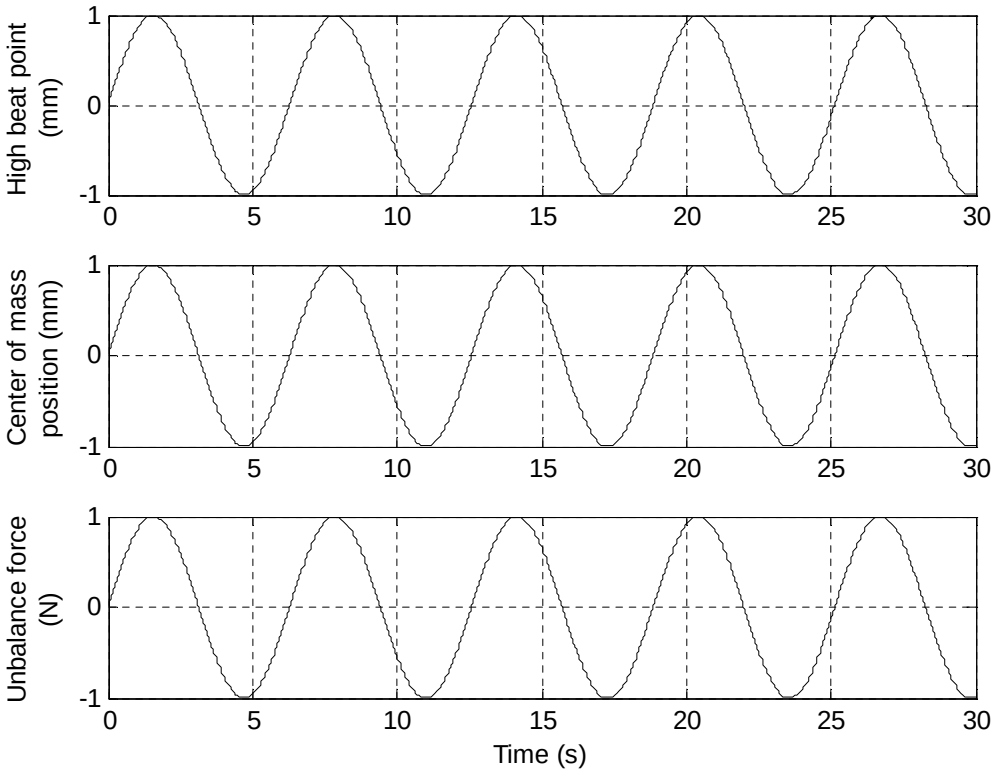

Figure 2.5 Time base plot for slow roll.

Figure 2.5 shows that for a slow rotational speed, high spot, center of mass and unbalance force are in same phase, in other words, along the same radial line on the rotor. With the speed increased to point designated by g_2, φ_2 on Figure 2.4, the phase of the center of mass and of the high spot become different. The difference of their phase is the angle φ_2 in Figure 2.4. In the time base plot in Figure 2.6, one can see that the unbalance

force and center of mass are in phase and the position of the high spot (high beat point) changed its phase.

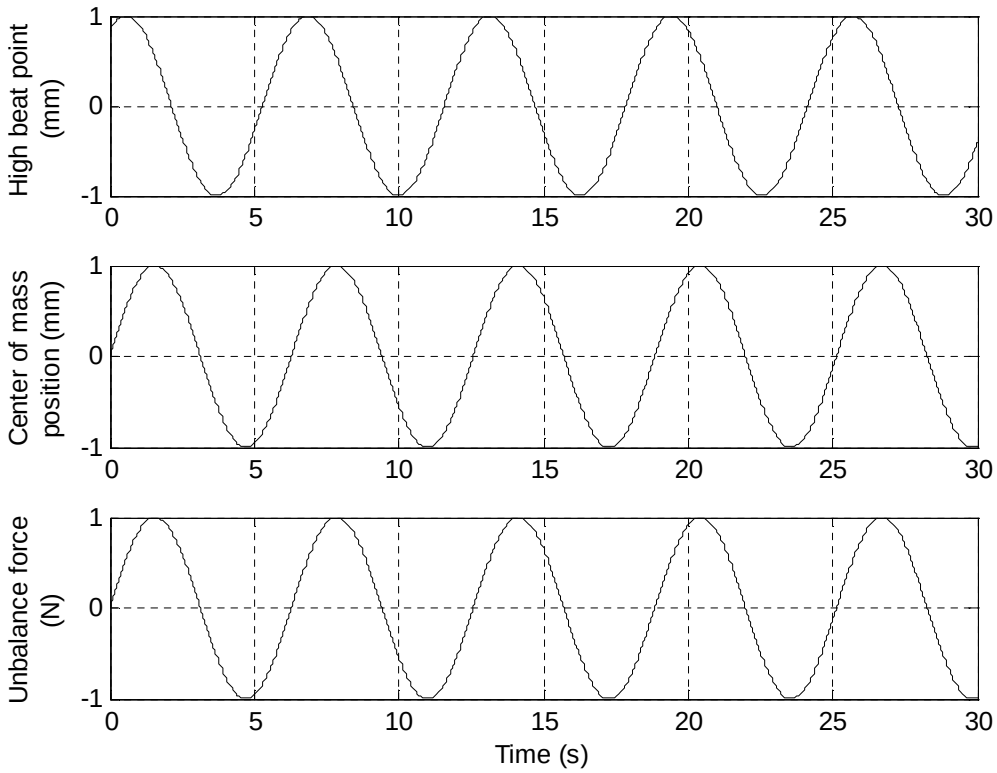

Figure 2.6 Time base plot for subcritical speed.

A cross section of the rotor and actuator is again shown in Figure 2.7, this time for a speed closer to resonance. The air gaps between the stator and rotor at the location of the center of mass - g_1 and the high spot - g_2, respectively, are now different. The air gap between the high beat point and stator g_2 is measured by sensors and reflected on the Bode plot. The air gap between the location of the center of mass and stator g_1 must be calculated. This can be done because the heavy spot is at a fixed angle with respect to the shaft.

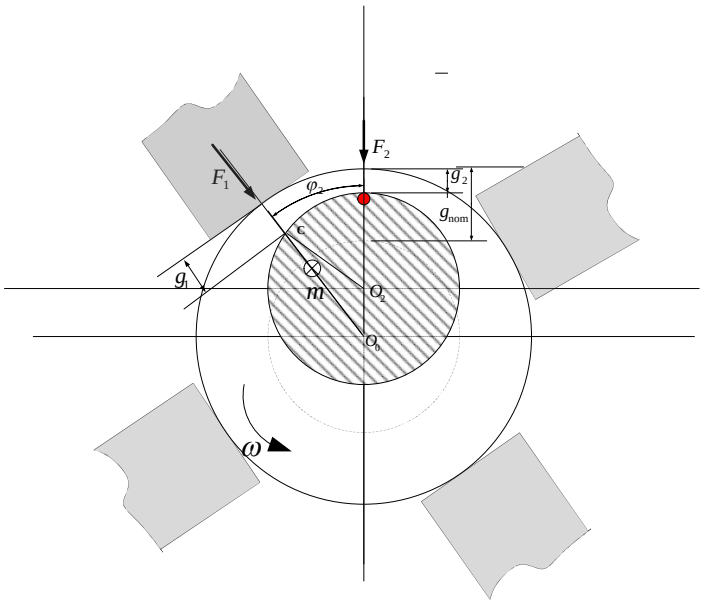

Figure 2.7 Position of the rotor at subcritical speed.

Starting from the cosine theorem:

$$a^2 = b^2 + c^2 - 2bc\cos\varphi \tag{2.2}$$

This means that the square of a side of a triangle equal to the sum of the squares of the two other sides, minus double the product of those sides by the cosine of the angle between them. Now look at the triangle O_0CO_2. Let the side O_0O_2 be marked with symbol b for the equation (2.2). Distance O_0O_2 is equal to the displacement of the geometrical center of the shaft and can be obtained experimentally and determined on the Bode plot. Let side O_2C be the side a; it is equal to the radius of the shaft r. Side O_0C can be the side c. Also, angle φ (known from the Bode plot as the phase), is the angle between a and b. Solving equation (2.2) for c we can calculate distance O_0C

$$c = \frac{2b(\cos\varphi) \pm \sqrt{2b\cos\varphi - 4(b^2 - a^2)}}{2} \tag{2.3}$$

Or $$O_0C = \frac{2O_0O_2\cos\varphi + \sqrt{(2O_0O_2\cos\varphi)^2 - 4({O_0O_2}^2 - r^2)}}{2} \tag{2.4}$$

And, knowing the nominal air gap g_{nom} and calculated distance O_0C we can determine the air gap g_1 which will be equal to:

$$g_1 = (g_{nom} + r) - O_0C \tag{2.5}$$

Substituting equation (2.4) in to (2.5) one can obtain a general formula for g_1:

$$g_1 = (g_{nom} + r) - \frac{2O_0O_2\cos\varphi + \sqrt{(2O_0O_2\cos\varphi)^2 - 4({O_0O_2}^2 - r^2)}}{2} \tag{2.6}$$

Note that from equation (2.5) one can see that the air gap at the location of the center of mass is a function of the radius of the rotor, nominal gap, displacement of the rotor, and phase φ.

Now substituting g_1 in to formula (2.1) in place of g one can calculate magnitude of the force F_1 that will be applied to the rotor at the point of the location of the center of mass:

$$F_1 = \frac{\varepsilon\mu_0 A_g N^2 I^2}{4(((g_{nom} + r) - \frac{2O_0O_2\cos\varphi + \sqrt{(2O_0O_2\cos\varphi)^2 - 4({O_0O_2}^2 - r^2)}}{2})^2)} \tag{2.7}$$

Now let's look how the force is changing in the high beat point or response point. The air gap g_2 (see Figure 2.7) can be determined from the experimental data using formula (2.8)

$$g_2 = (g_{nom} + r) - O_0O_2 \tag{2.8}$$

Where O_0O_2 is the amplitude of the vibration, or radial displacement, of the geometrical center of the shaft. Note that $g_1 \le g_2$. But the value of the injected current will change

due to changing phase of the injected sinusoidal wave with the rotating of the shaft. This phase also will be equal to the angle φ. So, the formula for the magnitude of the applied force F_2 at the point of response of the shaft or high beat point will be (2.9):

$$F_2 = \frac{\varepsilon \mu_0 A_g N^2 I^2}{4 g_2^{\,2}} \tag{2.9}$$

Substituting (2.8) into (2.9) the formula for calculating applied force at the high beat point can be obtained:

$$F_2 = \frac{\varepsilon \mu_0 A_g N^2 I^2}{4((g_{nom} + r) - O_0 O_2)^2} \tag{2.10}$$

As was mentioned above this force should compensate exciting force that is an unbalance force in this case.

MatLab codes were generated for observing this force graphically. The best performance of the rotor occurs when it rotates around its center of mass. From the plotted graphs, we can conclude that for obtaining the force that forces the rotor rotate around its center of mass, we need to generate a wave of current with a special shape for injecting into magnetic actuator.

Starting with the magnetic actuator force equation:

$$F = \frac{\varepsilon \mu_0 A_g N^2 I^2}{4 g_1^{\,2} \cos(\omega t + \varphi)} \tag{2.11}$$

It is desired to cancel the unbalance force, using the magnetic actuator force.

The equation for these forces can be stated thus:

$$ml\omega^2 \cos(\omega t) = \frac{\varepsilon \mu_0 A_g N^2 I^2}{4 g_1^{\,2} \cos(\omega t + \varphi)} \tag{2.12}$$

Solving for the current gives:

$$I^2 = \frac{ml\omega^2 \cos(\omega t) 4 g_1{}^2 \cos(\omega t + \varphi)}{\varepsilon \mu_0 A_g N^2} \tag{2.13}$$

Substituting (2.6) into (2.13) gives a formula for the ideal current that needs to be injected to cancel the unbalance exciting force:

$$I^2 = \frac{ml\omega^2 \cos(\omega t) 4 (g_{nom} + r - \frac{2O_0O_2 \cos\varphi + \sqrt{(2O_0O_2 \cos\varphi)^2 - 4(O_0O_2{}^2 - r^2)}}{2})^2 \cos(\omega t + \varphi)}{\varepsilon \mu_0 A_g N^2} \tag{2.14}$$

Finding the actual coil current is complicated by the switching nature of the opposing coils in the magnetic actuator. The top coil is "on" if, and only if, the bottom coil is "off" and vice versa. Also, the signal injection is interpreted as a negative current in a bottom coil. Finally the switch is made dictated by the expected direction of the unbalance force to be cancelled, as described in the formulas for all three conditions (2.15):

$$I = \begin{cases} \sqrt{\dfrac{ml\omega^2 \cos(\omega t) 4 g_1{}^2 \cos(\omega t + \varphi)}{\varepsilon \mu_0 A_g N^2}} & \text{when } \cos(\omega t) > 0 \\ -\sqrt{-\dfrac{ml\omega^2 \cos(\omega t) 4 g_1{}^2 \cos(\omega t + \varphi)}{\varepsilon \mu_0 A_g N^2}} & \text{when } \cos(\omega t) < 0 \\ 0 & \text{when } \cos(\omega t) = 0 \end{cases} \tag{2.15}$$

This is a complicated waveform, which is difficult to generate with conventional hardware. It is proposed to approximate this result with a single-frequency cosine wave because a cosine wave can be readily created using hardware common in the industry. Starting from the constraint of a cosine form wave, three parameters must be selected to define the injection, frequency, phase, and amplitude. To select frequency, a frequency

analysis of the ideal injection signal must be performed. The Figure 2.8 below is the Fast Fourier Transform of the idealized injection signal, using parameters taken from the experimental (which will be shown in Figure 2.10).

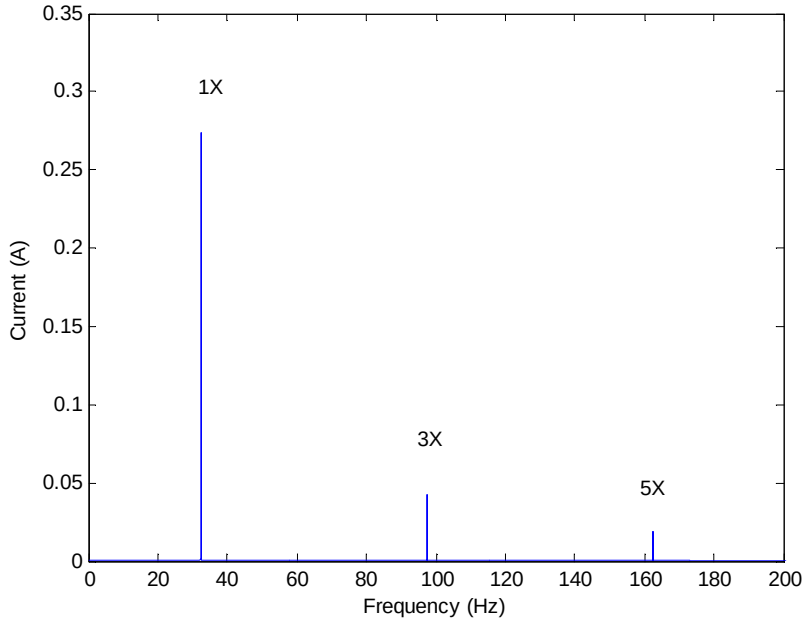

Figure 2.8 Frequency response of idealized unbalance compensation injection current for rotor running at 1950 RPM.

It is found that the dominant frequency component is that of the running speed. This is an intuitive result because the unbalance force, which is to be cancelled, occurs at this frequency. The phase between the unbalance force and the rotor response is found by the relationship between running speed and natural frequency, such that the magnetic force will always be in the opposite direction as the unbalance force. The amplitude of current injection is taken as the maximum amplitude of the idealized current injection.

The Figures 2.9 through 2.12 shows the ideal injection current found and a comparable cosine wave. The results for four running speeds are as follows: slow roll

(500 RPM); the speed that is used for the experiment (1,950 RPM); the critical speed (2,045 RPM); and super critical speed (2,152 RPM). The unbalance magnitude and rotor orbit amplitudes used in calculation are estimated from the response with no injection, which will be shown in Chapter IV. At a slow roll, the unbalance force is in phase with the rotor deflection and, therefore, the required current appears as simply the square root of a cosine wave. As the speed increases towards resonance, the rotor response approaches 90 degrees from the unbalance force. This phase shift results in the required current being an asymmetrical harmonic wave. Once resonance is passed, the required current moves back to a symmetrical pattern. Because of the switching of the top and bottom coils, there are always multiple frequency components in the current waveform.

Also, shown in the figures below is the proposed injection current. This is a cosine wave with an equivalent frequency as the running speed. It will be shown through simulation in the next section and experiments in Chapter IV that this proposed approach is capable of reducing rotor vibrations, even though it differs from the calculated current.

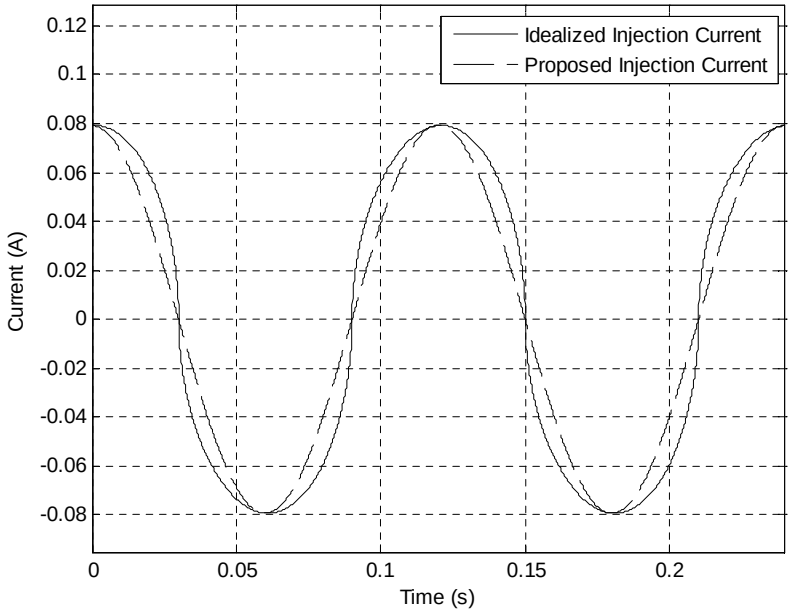

Figure 2.9 Calculated unbalance compensation current and proposed compensation current at slow roll (500 RPM).

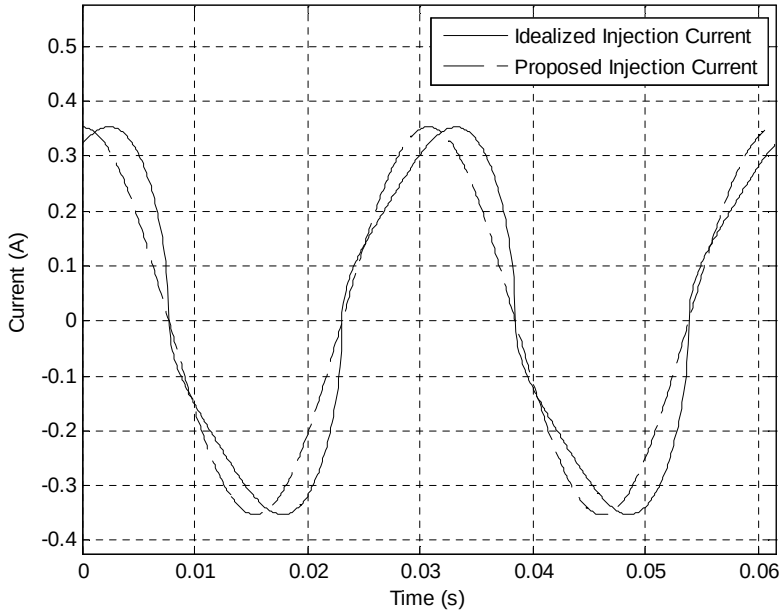

Figure 2.10 Calculated unbalance compensation current and proposed compensation current (1,950 RPM).

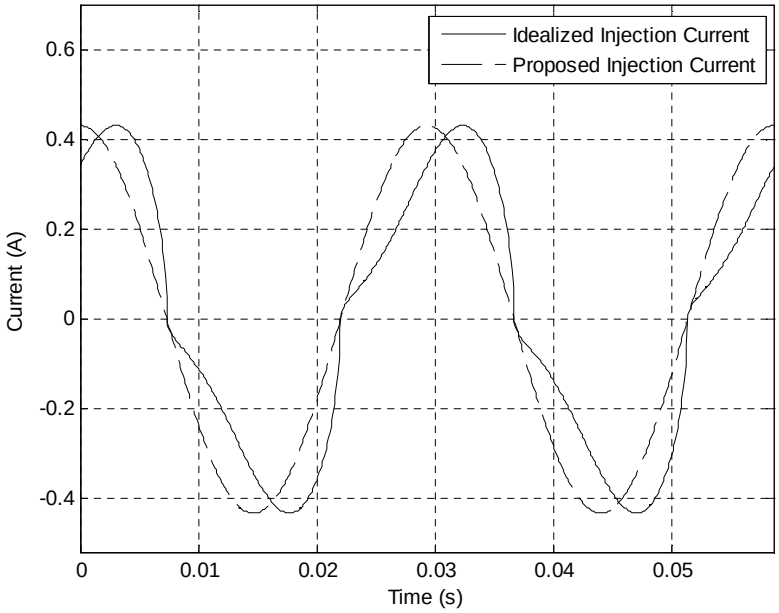

Figure 2.11 Calculated unbalance compensation current and proposed compensation current at critical speed (2,045 RPM).

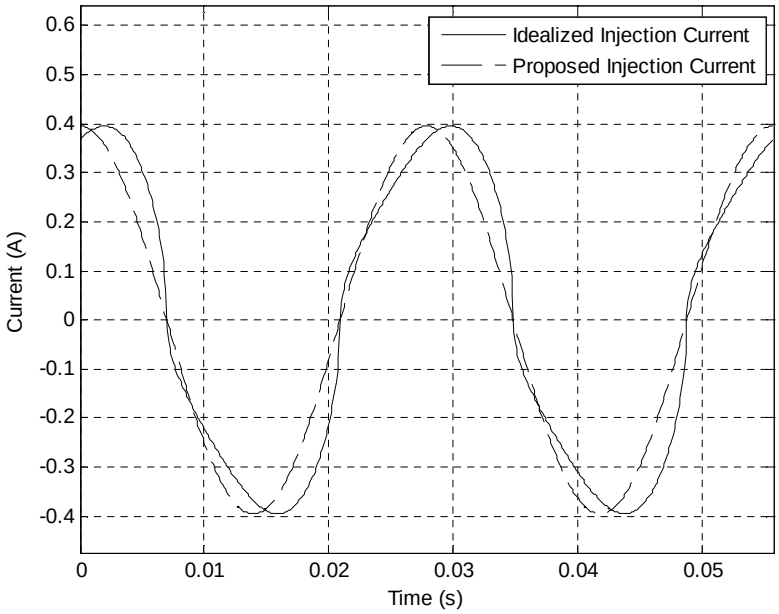

Figure 2.12 Calculated unbalance compensation current and proposed compensation current at supercritical speed (2,152 RPM).

2.3 Method of Solution and Numerical Simulation Results

A simulation is conducted to demonstrate the vibration control method described in the previous section and to make predictions of the results of the experiment discussed in Chapter 4. The experimental rotor (the geometry of which is discussed in later chapters) is modeled using Timoshenko beam elements. Force is applied to certain nodes in the form of a position feedback stiffness to account for the bushing supports. The rotor-exciter system is simulated in MatLab Simulink, using Runge-Kutta numerical integration. Figure 2.8 below shows the Simulink model.

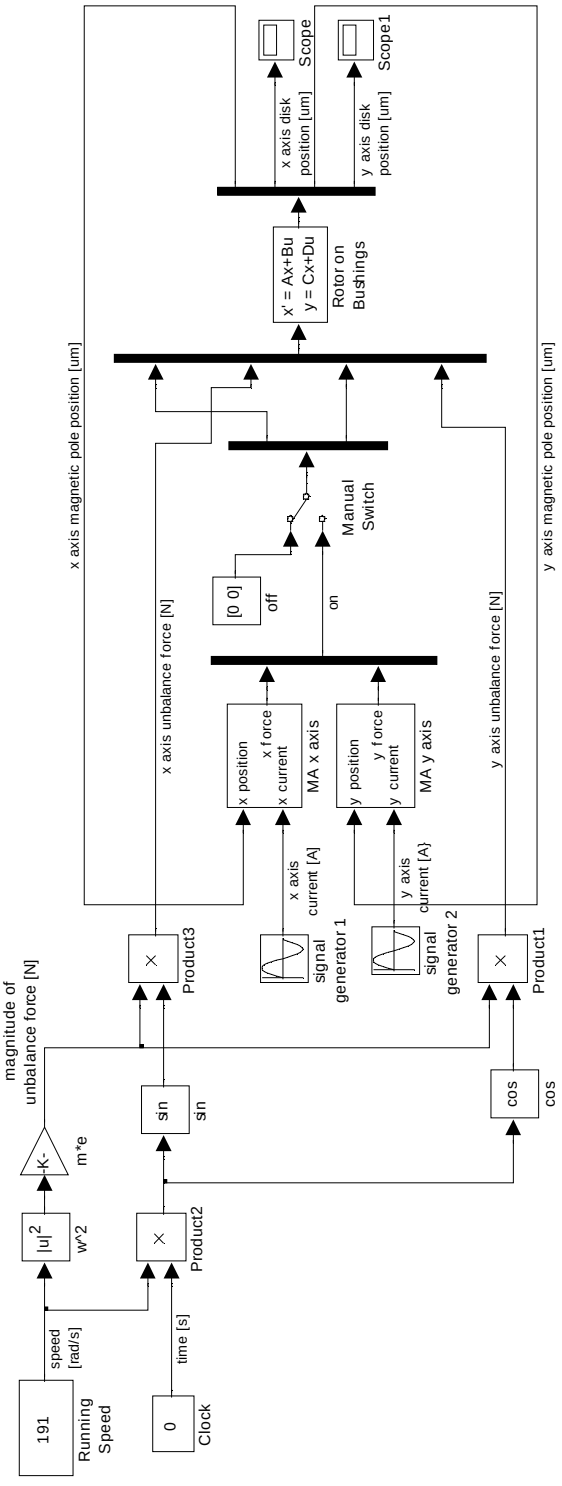

Figure 2.13 Simulink model for numerical simulation of flexible rotor with unbalance and magnetic actuator compensation.

In the simulation, the rotor running speed and eccentricity create an unbalance force which acts only at the disk node. The unbalance force acts in vertical and horizontal directions 90º out of phase. The magnitude of the unbalance is estimated from the orbit of the actual rotor without vibration control as 1.68 gm-in. There is also a representation of the magnetic actuator which may be turned "off" or turned "on" by removing or applying its resulting force from the rotor via a manual switch block. Each axis of the magnetic actuator is modeled using the nonlinear equation (2.15) for the top and bottom magnetic coils in opposite directions. This is in blocks "MA x axis" and "MA y axis" for the horizontal and vertical axis, respectively. Also, note that the rotor position is a factor in the magnetic actuator force, which is taken from the magnetic pole node of the finite element rotor. Figure 2.14 below shows the inside of one magnetic actuator axis block. The saturation blocks mimic the real system, which does not accept negative current.

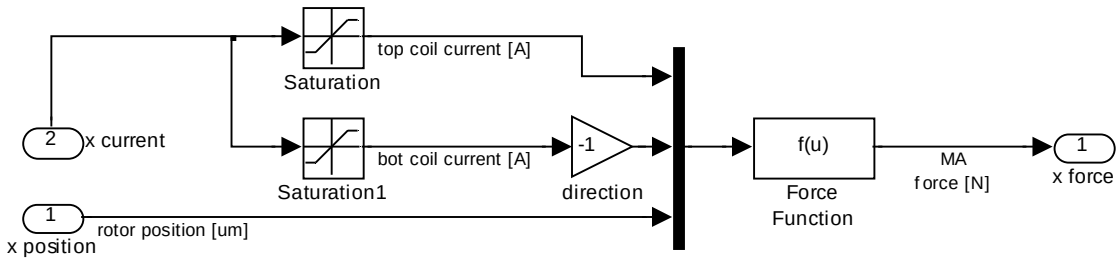

Figure 2.14 Simulink model of magnetic actuator force corresponding to block "MA x axis" shown in Figure 2.8.

The current generators are set for sinusoidal signals with the same frequency as rotation and out-of-phase. The current from each generator is shown in Figure 2.15 below.

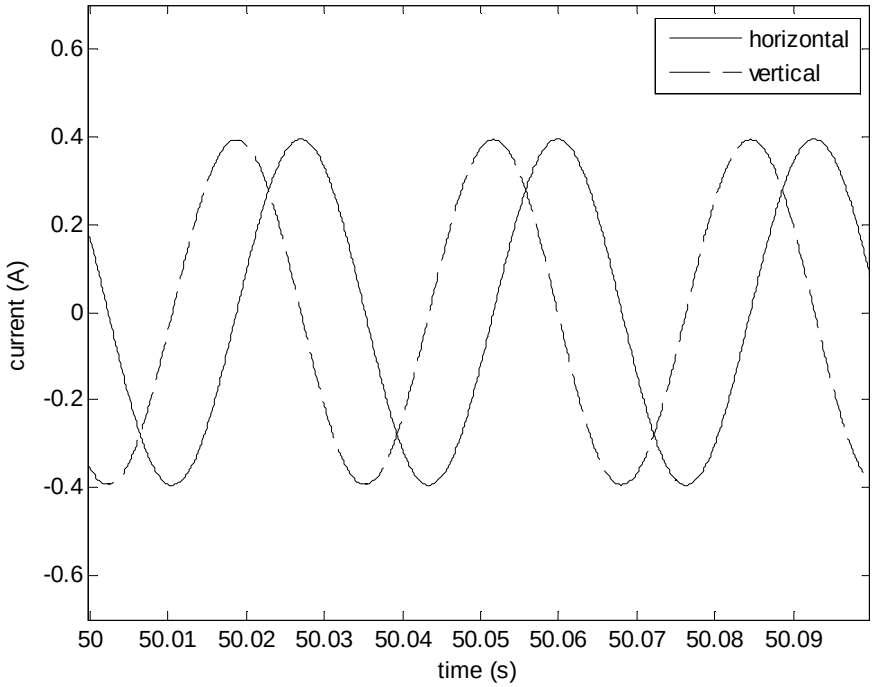

Figure 2.15 Sample of current signals sent to magnetic actuator in simulation.

The simulation was first run with the actuator force turned "off" and allowed to come to steady state rotation. The position of the disk in the horizontal and vertical directions for a characteristic span of time is shown in Figure 2.16. Note that deflection in each direction has slightly different amplitude due to non-isotropic bearing stiffness.

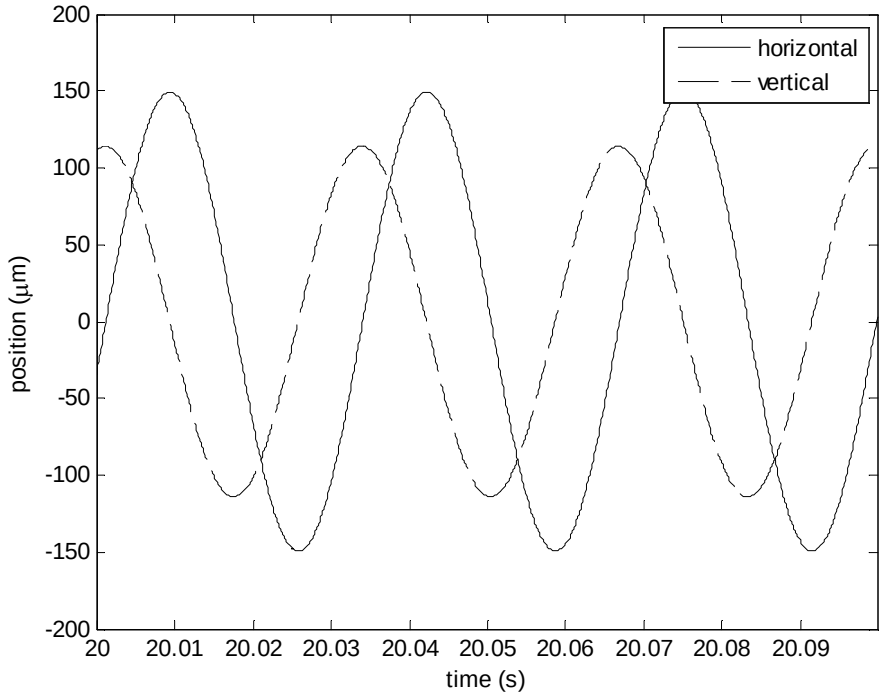

Figure 2.16 Simulated vibration of rotor at disk in horizontal and vertical directions with no vibration control.

After a time, the magnetic actuator is switched to "on." The vibrations of the rotor due to unbalance are decreased. Figure 2.17 shows the rotor vibrations at the disk now with vibration control. Note the change of scale.

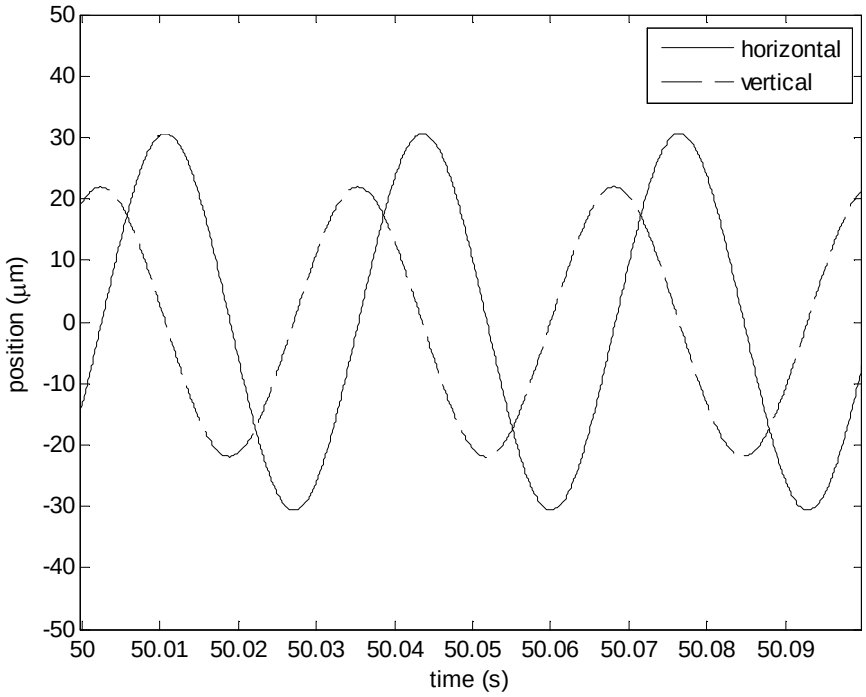

Figure 2.17 Simulated vibration of rotor at disk in horizontal and vertical directions with vibration control.

For comparison, Figure 2.18 below shows the orbit at the disk before and after vibration control is applied. A vibration reduction of 78% is achieved through use of the magnetic actuator.

Larger reductions in the experiment were achieved. However, it was found that this caused problems when passing through transient vibrations. If the magnitude of the transient vibration happens to be larger than the residual vibrations at steady state, then for a short period of time the actuator having a fixed phase, will be forcing the vibrations larger. Using this nonlinear numerical simulation, it is observed that these short-moment cases are capable of forcing the rotor outside of the actuator's effective geometric operational range. This causes unstable vibrations. Because of this, there is a limitation of how much the vibrations can be canceled.

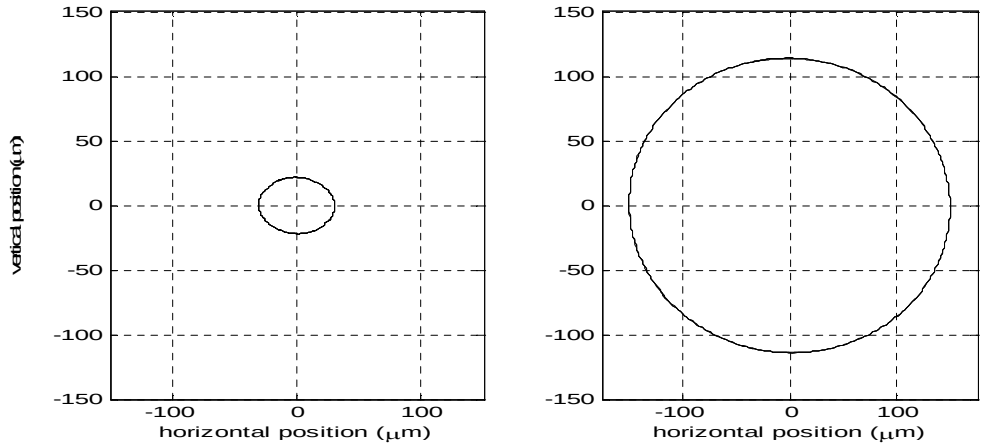

Figure 2.18 Simulated rotor orbit at the disk with vibration control (left) and with no vibration control (right).

CHAPTER III

THE FLEXIBLE ROTOR TEST RIG

3.1 Overview of the rig

The experiment was performed using a commercial Bently Nevada Rotor Kit RK4 shown in (Figure 3.1(a)) and a modified active magnetic bearing (AMB) manufactured by SKF Magnetic Bearings see (Figure 3.2(b)). The modified bearing serves as an actuator. The Bently Nevada Corporation Rotor Kit is a versatile and compact example of a rotating machine that demonstrates several patterns of shaft vibration by duplicating vibration-producing phenomena found in large rotating machinery. This combination of RK4 and AMB was found effective in demonstrating one of the features of active magnetic actuators with vibration control.

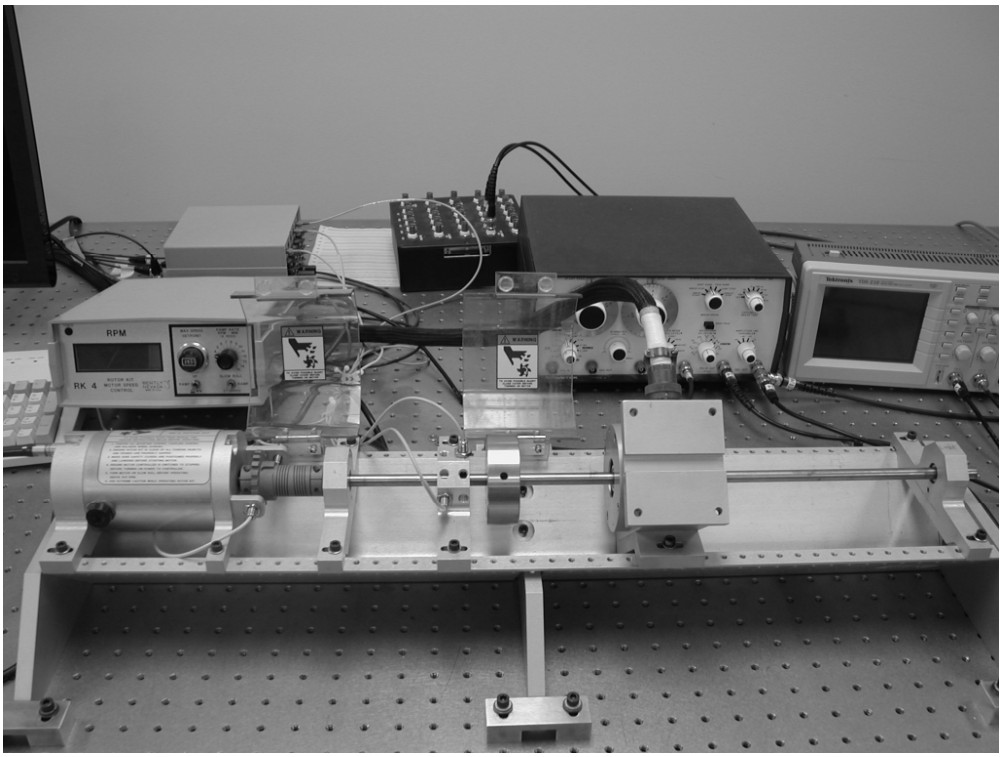

Figure 3.1(a) Bently Nevada Rotor Kit RK4 with active magnetic actuator.

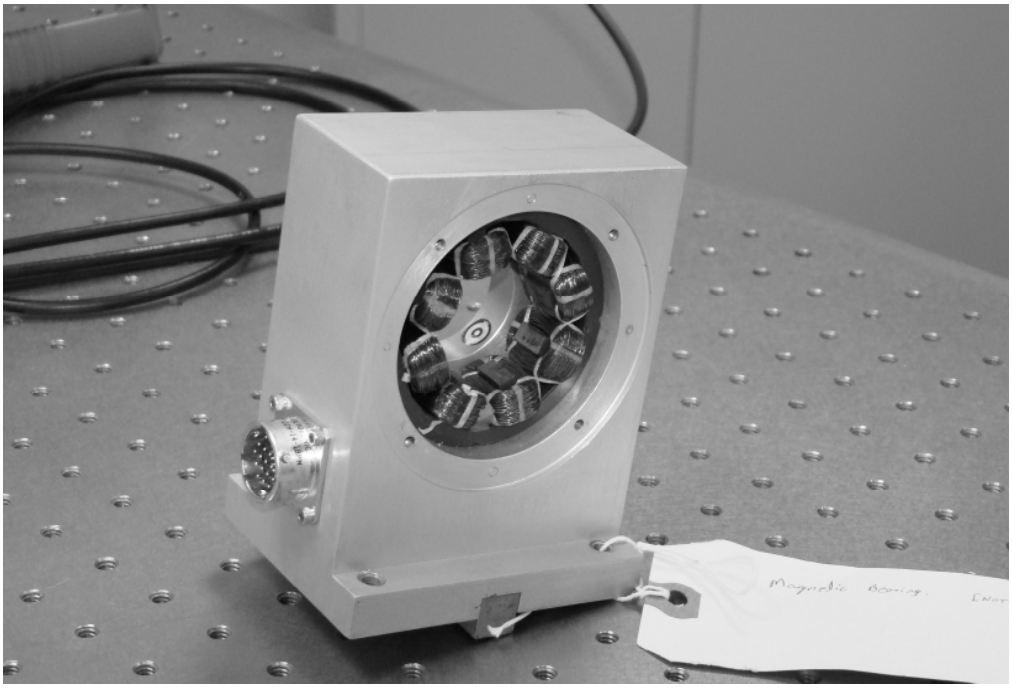

Figure 3.1(b). Active magnetic actuator by SKF Magnetic Bearings.

In addition to active magnetic actuator (AMA) sensors, a Bently Nevada Rotor Proximitor Assembly was used. Signals were transmitted first to a Bently Nevada Data Acquisition Interface Unit (DAIU) and then to the Bently Nevada Automated Diagnostics for Rotating Equipment software (ADRE for Windows) for displaying and recording the data collected from the probes. The probes are located near the disk with one probe in the vertical and one in the horizontal directions.

The stainless steel shaft is 560 mm long (22 in) and 10 mm (0.394 in) in diameter. The weight of the rotor shaft is 350 g. One steel balance disk, 76.2 mm (3 in) in diameter, 25.4 mm (1 in) thick and weight of 0.8 kg (1.764 lb), was attached at approximately one quarter of the rotor span from the motor side. The rotor supported by two bearings. The radial rotor of the active magnetic actuator, which is 34.3 mm (1.35 in) in diameter, 47.8 mm (1.88 in) long and weight of 0.264 kg (0.58 lb), is placed at the bearings midspan. The rotor was driven by an electrical motor with a separate controller. The rotor is attached to the motor by a flexible aluminum coupling, which also incorporates speed sensors for motor control and a Keyphasor for rotor's angle determination.

The speed is controlled by feedback pulses from speed sensors, which observes a 20-notch wheel mounted on the rotor coupling. The motor controller let us choose desired rotational speed that can be selected from 250 rpm to 10,000 rpm. In addition, the speed set point can be set to ramp up or downward at a rate of up to 15,000 rpm/min. The radial displacement of the shaft was measured in two planes (vertical and horizontal) with eddy current transducers or proximity probes. Proximity probes measure distances between 0.254 mm (10 mils) and 2.28 mm (90 mils). The proximity probes signal is generated by measuring voltage changes in the proximity probes circuit. The Keyphasor let us know

the angular location (phase) of the shaft vibration response in relation to the physical location of the event (Figure 3.2). Also, we used a keyphasor for triggering a Wavetek 5MHz LIN/LOG sweep generator that produced an injected sine wave, to be described later in this chapter.

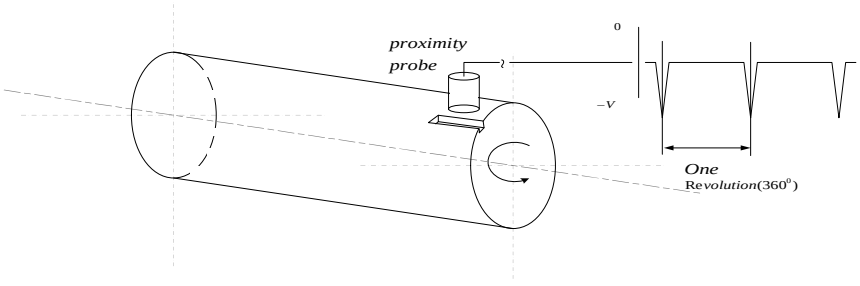

Figure 3.2 Keyphasor sensor used to determine the phase.

3.2 Redesign of active magnetic actuator

An active magnetic actuator (AMA) was used for vibration control, its specification presented in Appendix C.

The AMA system consists of a stator, a rotor with an internal collet, position sensors, touchdown bearing, a control system and power amplifiers. The rotor, which is made of laminated iron, is attached the shaft with the collet. The magnetic actuators and sensors are located on opposite sides of the rotor in two perpendicular control axes. The control system and amplifiers are located in a separate housing and connected by wires. The stator is also made of laminated steel with poles on the internal diameter. Wire coils are wound around each pole, so that the actuator is divided into four quadrants, each having two poles. In our case, quadrants are aligned strictly vertically and horizontally.

Opposing quadrants constitute an axis and, therefore, each actuator can be described by two perpendicular axes. So each actuator's axis has a pair of amplifiers to provide current to generate an attractive magnetic force to correct the position of the rotor along that particular axis. The amplifiers, which are of pulse with modulation (PWM) type, are high voltage switches that are turned "on" and "off" at a high frequency, to achieve a current in the coils requested by the controller. The stator and rotor are the active bearing elements used to apply force to the shaft. The application of magnetic actuators is based upon the principle that an electromagnet will attract ferromagnetic material. The sensor ring measures radial position of the shaft and is mounted as close to the actuator as possible. The sensors feed information about the position of the shaft to the controller in the form of an electrical voltage. The touchdown bearing is not in contact with the rotor during normal operation and used to protect the magnetic poles when vibration of the shaft exceeds admissible level. See Figure3.3, which shows the components disassembled. The touchdown bearing used on this are deep groove ball bearings mounted in the actuator housing. The clearance between the shaft and the touchdown bearing is approximately half of that between the magnetic bearing rotor and stator. The original magnetic bearing was designed for 3/8 inch diameter shaft. Bently Nevada's Rotor Kit RK4 uses a shaft 10mm in diameter. To keep the same clearance between the shaft and the touchdown bearing, a new bearing ring with necessary dimensions was produced.

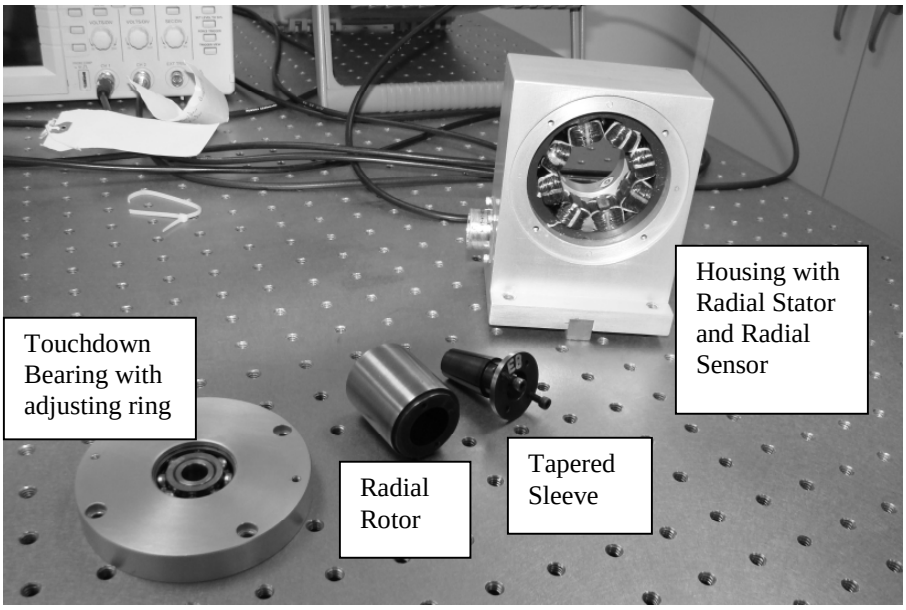

Figure 3.3 Components of the active magnetic actuator.

As was mentioned above, a V-shape base from Bently Nevada was used. A special V-shape mount was designed and manufactured for mounting the active magnetic actuator by Revolve Magnetic Bearings, Inc. The V-shape mount is shown in Figure 3.4. Since the V-shape rotor kit's base is being perturbed by an unbalance force in the X-Y plane, there always is a harmonic force applied in the vertical and horizontal directions, no matter where the perturbation plane is. But it is possible to reduce the torque on the base by reducing the length of the moment arm between the perturbation force (unbalance at the disk) and the center of mass of the base.

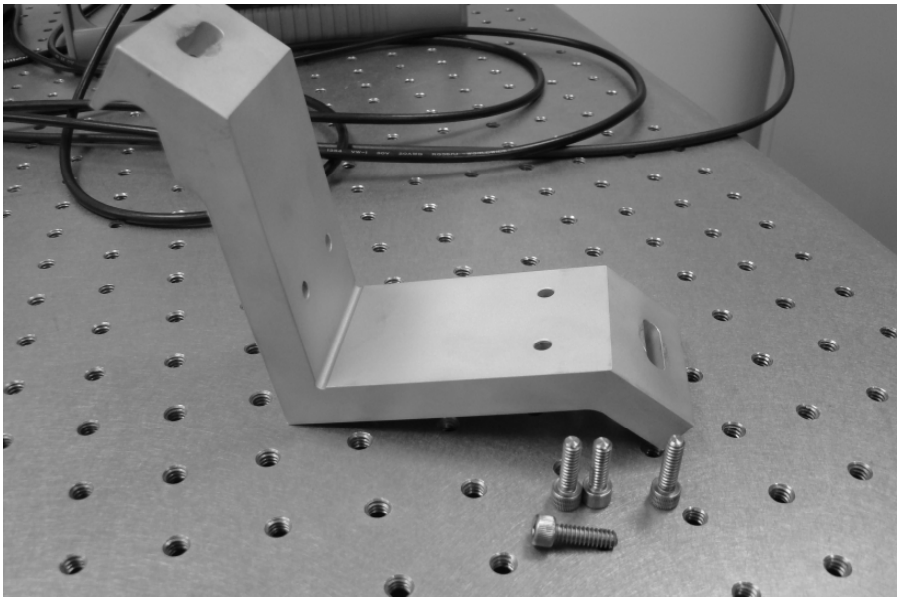

Figure 3.4 V-shape actuators mount.

Since the v-shape base is symmetric about the Y-Z plane (see Figure 3.5), we have only vertical and axial offsets that caused angular moments. The axial location of the unbalance force is the consequence of the location of the rotor components. So, rotor response is different in vertical and horizontal direction not only due to the gravity but also to the vibration of the base caused by angular moments (to be shown later in thesis).

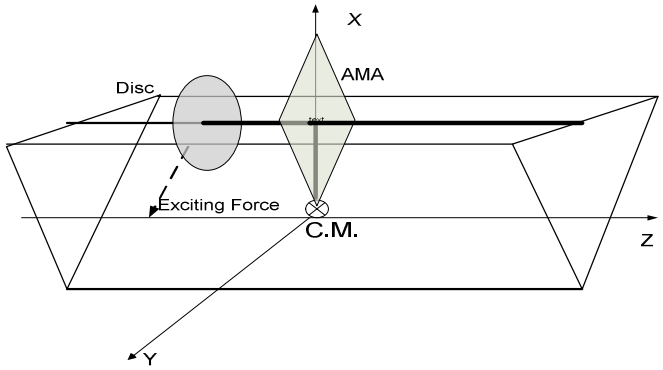

Figure 3.5 V-shape base schemes.

To minimize these moments as much as possible, the mount was designed to keep the center of mass of the rig as close to the axis of rotation as possible. See Figure 3.6.

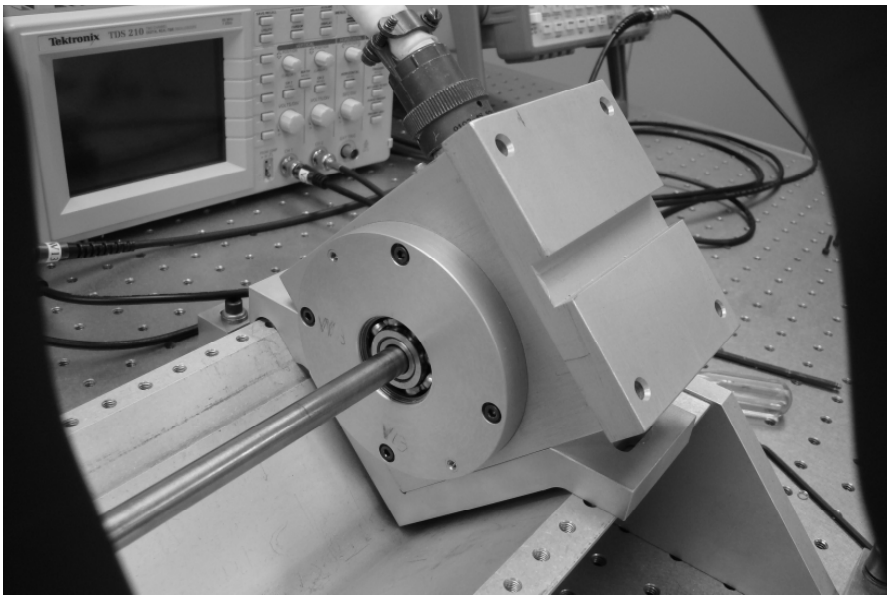

Figure 3.6 Active magnetic actuator assembled on a V-shape base.

The active magnetic actuator was connected to the MB350 Controller. See Figure 3.7. The MB350 Controller is a self-contained, fully digital, magnetic bearing control system. It has a great number of features. But, to make this method of reducing vibration more attractive and easy to use, only a simple one is used. The function of the controller is to receive and process the voltage signal from the position sensors and inject and calculate a feedback control current. Here it is used for accepting and sending externally-generated harmonic current to the active magnetic actuator. The MB350 controller was connected to the computer via MBScope software. MBScope is a Windows-based software program designed to provide full access to the functional capabilities of SKF magnetic bearing controllers. System parameters such as position and current can be monitored with an external computer connected with a parallel cable. The software provides a rich,

graphical interface for viewing this information. MBScope software can also be used for control law parameter adjustment (tuning), code loading, and detailed fault analysis.

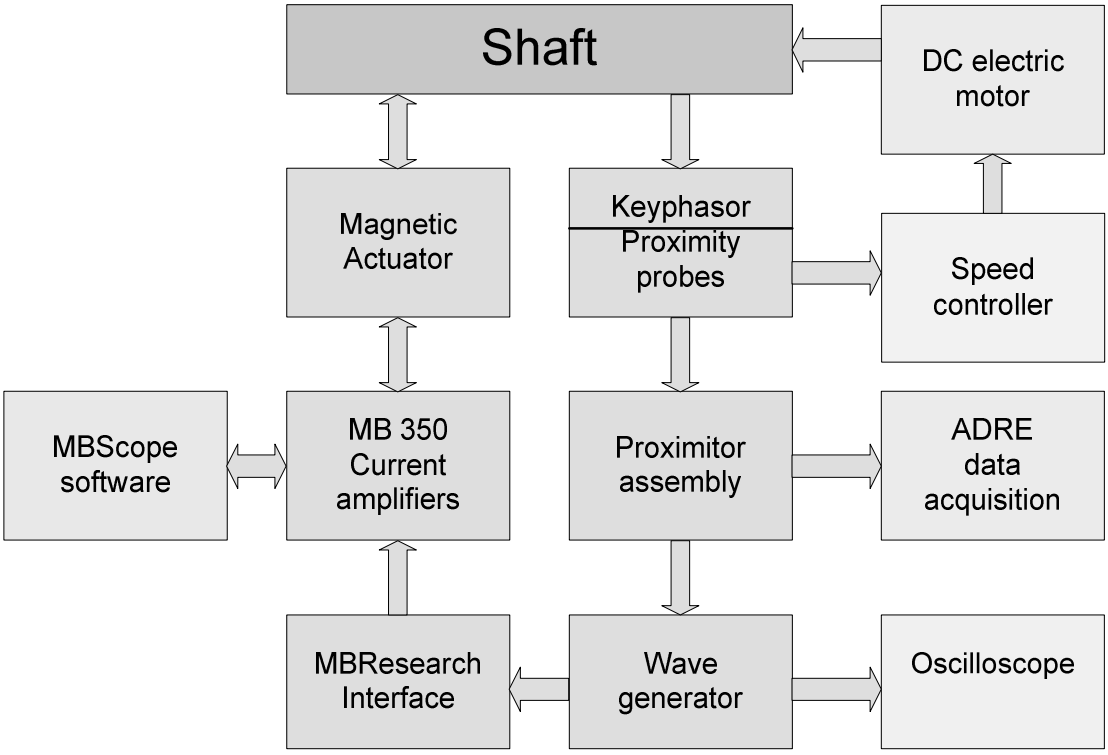

Figure 3.7 Scheme of connection of the rig.

Two Wavetek sweep/function generators are connected to the MB350 Controller through a MBResearch board. The MBResearch is a BNC connector-based breakout box that provides access to signals from the magnetic bearings controllers. The signals available include analog current and position signals, and top dead centre (TDC) pulse signal for monitoring speed and phase. In addition, MBResearch provides the ability to inject signals on all control axes, making the rig an excellent research tool in the areas of control theory and rotor dynamics. The last feature was used in this experiment. The

MBResearch board connects to the magnetic actuator controller via 68-pin SCSI connector.

Two Wavetek sweep/function generators are taken for generating and injecting sine waves in the vertical and horizontal directions. Model 185 and model FG3B are used in this experiment. Wavetek generators are a precision source of sine, triangle square, positive pulse and negative pulse waveforms as well as a DC voltage supply. The frequency of the waveforms is manually or remotely variable from $100\,\mu Hz$ to $5\,\mu Hz$. Frequencies can be swept both linearly and logarithmically. The amplitude of the waveforms is variable from 20V p-p, open circuit maximum, to -80dB. The waveforms can be given a DC offset positively and negatively. The symmetry of the waveforms is continuously adjustable from approximately 1:19 to 19:1. Varying symmetry provides variable duty cycle pulses, sawtooth and asymmetrical sine waveforms. The heart of the generator consists of the positive and negative current sources, the current switch, timing capacitors, triangle amplifier, and hysteresis switch. The positive and negative current sources generate equal but opposite polarity currents, which charge and discharge the timing capacitor selected by the range selector. The current switch, which is controlled by the hysteresis switch, selects either the positive or negative current as the input to the capacitor. Since the capacitor is being charged by a current source, which changes polarity periodically, the voltage across the capacitor forms a triangle waveform and reaches predetermined positive and negative peak values. When this occurs, the output of the hysteresis changes state and causes the current switch to select the opposite polarity current. The output of the hysteresis switch is a square wave whose edges correspond to the triangle peak values. The magnitude of the current produced by the current sources is

dependent upon the output of the voltage controlled generator (VCG) amplifier. By varying the output of the VCG amplifier, the frequency of the triangle and square waveforms may be controlled. In order to generate sine waves, the triangle waveform is sine shaped in the sine converter circuit with nonlinear elements. The waveforms switch selects the waveform of interest and the portion of the signal is selected by the amplitude potentiometer and applied to the output amplifier. The output amplifier is capable of driving a 50Ω load and may be DC offset. The amplifier output is routed to a 50Ω attenuator which can provide 60dB of attenuation in 20dB steps. An additional 20dB of attenuation can be obtained from the amplitude control. We used the generator in the trigger mode. In the trigger mode, the generator is stopped by the amplifier. This amplifier compares the output of the triangle amplifier to ground. Its output draws just the right amount of current away from the capacitor to keep it at zero volts. This level is known as the “trigger baseline”. When the external signal is applied to the trigger input, it is shaped into a fast rise time pulse by squaring the circuit and is applied to the trigger logic circuit. This circuit in turn shuts off the trigger amplifier for one cycle of the output waveform [22].

The wave generators are triggered by the signal received from the Bently Nevada Rotor Kit Proximitor Assembly. That signal is taken from the Keyphasor probe. Also this signal was sent to the interface and then to an independent data acquisition system.

An Automated Diagnostics for Rotating Equipment (ADRE) system was used. The ADRE system is specifically designed for real-time highly parallel signal processing and presentation. This system incorporates the functionality of many types of instrumentation, such as oscilloscopes, spectrum analyzers, filters, signal conditioners, and digital

recorders into a single platform. The system's real-time display capability permits it to continuously display data independently of data being stored to permanent memory. An ADRE data acquisition system consists of a Bently Nevada 408 Dynamic Signal Processing Instrument, ADRE client software, and a computer capable of running ADRE software. The Bently Nevada data acquisition interface unit (DAIU) 408 supports many standard and non-standard input types, including both dynamic transducer signals (such as those from proximity probes), and static transducer signals (such as process variables from transmitters and distributed control systems). For rotating machinery, a Keyphasor or other speed input signal can be used. A Keyphasor with a 1 TDC mark is used for phase and a speed sensor with a 28 teeth is used for speed.

Also, we used a Tektronix TDS210 oscilloscope for observation and synchronization. The Tektronix TDS210 oscilloscope is a graph-displaying device. It draws a graphical representation a voltage signal. In most applications, the graph shows how signals change over time: The vertical axis represents voltage and the horizontal axis represents time. A third axis is indicated by the intensity or brightness of the display.

The Tektronix TDS210 oscilloscope's simple graph can tell many things about a signal such as:

- The time and voltage values of a signal.
- The frequency of an oscillating signal.
- The "moving parts" of a circuit represented by the signal.
- The frequency with which a particular portion of the signal is occurring relative to, other portions.

- Whether or not a malfunctioning component is distorting the signal
- How much of a signal is direct current (DC) or alternating current (AC) and how much of the signal is noise.
- Whether the noise is changing with time.

The specification for the Tektronix TDS 210 oscilloscope is presented in Table 3.3.

3.3 Rotordynamic modeling

Mathematical modeling is done in order to estimate the parameters of the mechanical system such as unbalance and to validate the assumptions made in Chapter II. Finite element analysis is applied in modeling of the rotor-bearing system using the finite element modeling software. A Campbell diagram is drawn and the calculation of critical speeds and mode shapes for the rotor on journal bearings (and with active magnetic actuator off) are made. A determination of the magnitude of the unbalance is made by assuming static unbalance at the disk and tuning orbit to experimental data. Also included are the prediction of static deflection of the rotor and the critical speed map.

The finite element model consists of 53 Timoshenko beam elements with eight degrees of freedom each and takes into account rotational inertia and shear deformation. The model is shown in Figure 3.8.

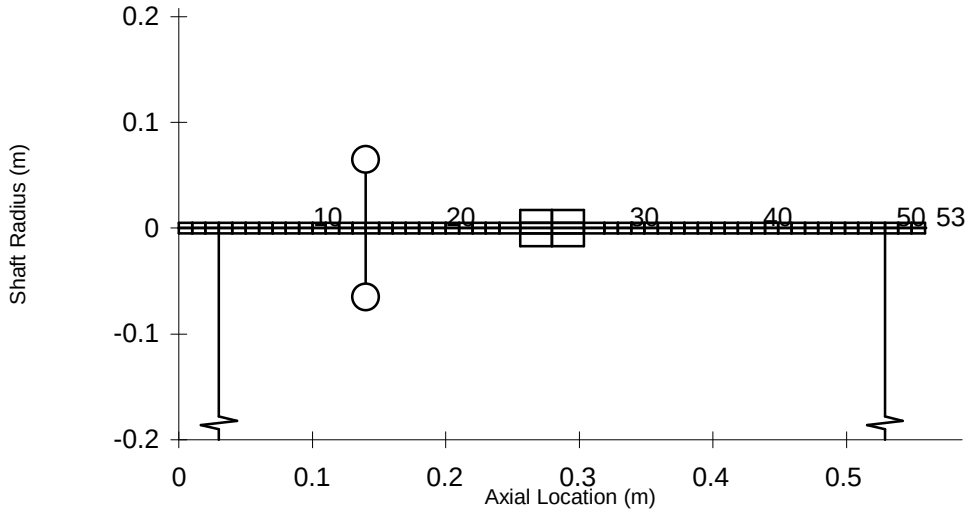

Figure 3.8 Finite element model of rotor.

The finite element model used for the configuration of the shaft is 560 mm long (22 in) and 10 mm (0.394 in) in diameter and is supported by journal bearings. One steel balance disk, 76.2 mm (3 in) in diameter, 25.4mm (1 in) thick, and 0.8 kg (1.764 lb) is attached to the shaft at approximately one quarter of the bearing span (on the motor side). The rotor of the radial active magnetic actuator is 34.3mm (1.35 in) in diameter, 47.8 mm (1.88 in) long and has a mass of 0.264 kg (0.58 lb). The actuator rotor is placed on the rotor at the bearing midspan. The detailed geometry (FEA input file) is presented in Table II. The Campbell diagram for the rotor is shown in Figure 3.9.

Table I. Finite element analysis input file.

Station	Length	OD	ID	Density	Elastic Modulus	Shear Modulus	Added Weight	Added Ip	Added It
#	m	m	m	kg/m^3	N/m^2	N/m^2	kg	$kg\text{-}m^2$	$kg\text{-}m^2$
1	0.01	0.01	0	7861.093	1.928E+11	6.573E+10	0	0	0
2	0.01	0.01	0	7861.093	1.928E+11	6.573E+10	0	0	0
3	0.01	0.01	0	7861.093	1.928E+11	6.573E+10	0	0	0
4	0.01	0.01	0	7861.093	1.928E+11	6.573E+10	0	0	0
5	0.01	0.01	0	7861.093	1.928E+11	6.573E+10	0	0	0
6	0.01	0.01	0	7861.093	1.928E+11	6.573E+10	0	0	0
7	0.01	0.01	0	7861.093	1.928E+11	6.573E+10	0	0	0
8	0.01	0.01	0	7861.093	1.928E+11	6.573E+10	0	0	0
9	0.01	0.01	0	7861.093	1.928E+11	6.573E+10	0	0	0
10	0.01	0.01	0	7861.093	1.928E+11	6.573E+10	0	0	0
11	0.01	0.01	0	7861.093	1.928E+11	6.573E+10	0	0	0
12	0.01	0.01	0	7861.093	1.928E+11	6.573E+10	0	0	0
13	0.01	0.01	0	7861.093	1.928E+11	6.573E+10	0	0	0
14	0.01	0.01	0	7861.093	1.928E+11	6.573E+10	0	0	0
15	0.01	0.01	0	7861.093	1.928E+11	6.573E+10	0.8	0.0006	0.000334
16	0.01	0.01	0	7861.093	1.928E+11	6.573E+10	0	0	0
17	0.01	0.01	0	7861.093	1.928E+11	6.573E+10	0	0	0
18	0.01	0.01	0	7861.093	1.928E+11	6.573E+10	0	0	0
19	0.01	0.01	0	7861.093	1.928E+11	6.573E+10	0	0	0
20	0.01	0.01	0	7861.093	1.928E+11	6.573E+10	0	0	0
21	0.01	0.01	0	7861.093	1.928E+11	6.573E+10	0	0	0
22	0.01	0.01	0	7861.093	1.928E+11	6.573E+10	0	0	0
23	0.01	0.01	0	7861.093	1.928E+11	6.573E+10	0	0	0
24	0.01	0.01	0	7861.093	1.928E+11	6.573E+10	0	0	0
25	0.0155	0.01	0	7861.093	1.928E+11	6.573E+10	0	0	0
26	0.0239	0.01	0	7861.093	1.928E+11	6.573E+10	0	0	0
26	0.0239	0.034	0.01	7639.654	1.928E+11	6.573E+10	0	0	0
27	0.0239	0.01	0	7861.093	1.928E+11	6.573E+10	0	0	0
27	0.0239	0.034	0.01	7639.654	1.928E+11	6.573E+10	0	0	0
28	0.0155	0.01	0	7861.093	1.928E+11	6.573E+10	0	0	0
29	0.01	0.01	0	7861.093	1.928E+11	6.573E+10	0	0	0
30	0.01	0.01	0	7861.093	1.928E+11	6.573E+10	0	0	0
31	0.01	0.01	0	7861.093	1.928E+11	6.573E+10	0	0	0
32	0.01	0.01	0	7861.093	1.928E+11	6.573E+10	0	0	0
33	0.01	0.01	0	7861.093	1.928E+11	6.573E+10	0	0	0
34	0.01	0.01	0	7861.093	1.928E+11	6.573E+10	0	0	0
35	0.01	0.01	0	7861.093	1.928E+11	6.573E+10	0	0	0
36	0.01	0.01	0	7861.093	1.928E+11	6.573E+10	0	0	0
37	0.01	0.01	0	7861.093	1.928E+11	6.573E+10	0	0	0
38	0.01	0.01	0	7861.093	1.928E+11	6.573E+10	0	0	0
39	0.01	0.01	0	7861.093	1.928E+11	6.573E+10	0	0	0
40	0.01	0.01	0	7861.093	1.928E+11	6.573E+10	0	0	0
41	0.01	0.01	0	7861.093	1.928E+11	6.573E+10	0	0	0
42	0.01	0.01	0	7861.093	1.928E+11	6.573E+10	0	0	0
43	0.01	0.01	0	7861.093	1.928E+11	6.573E+10	0	0	0
44	0.01	0.01	0	7861.093	1.928E+11	6.573E+10	0	0	0
45	0.01	0.01	0	7861.093	1.928E+11	6.573E+10	0	0	0
46	0.01	0.01	0	7861.093	1.928E+11	6.573E+10	0	0	0
49	0.01	0.01	0	7861.093	1.928E+11	6.573E+10	0	0	0
50	0.01	0.01	0	7861.093	1.928E+11	6.573E+10	0	0	0
51	0.01	0.01	0	7861.093	1.928E+11	6.573E+10	0	0	0
52	0.01	0.01	0	7861.093	1.928E+11	6.573E+10	0	0	0
53	0								

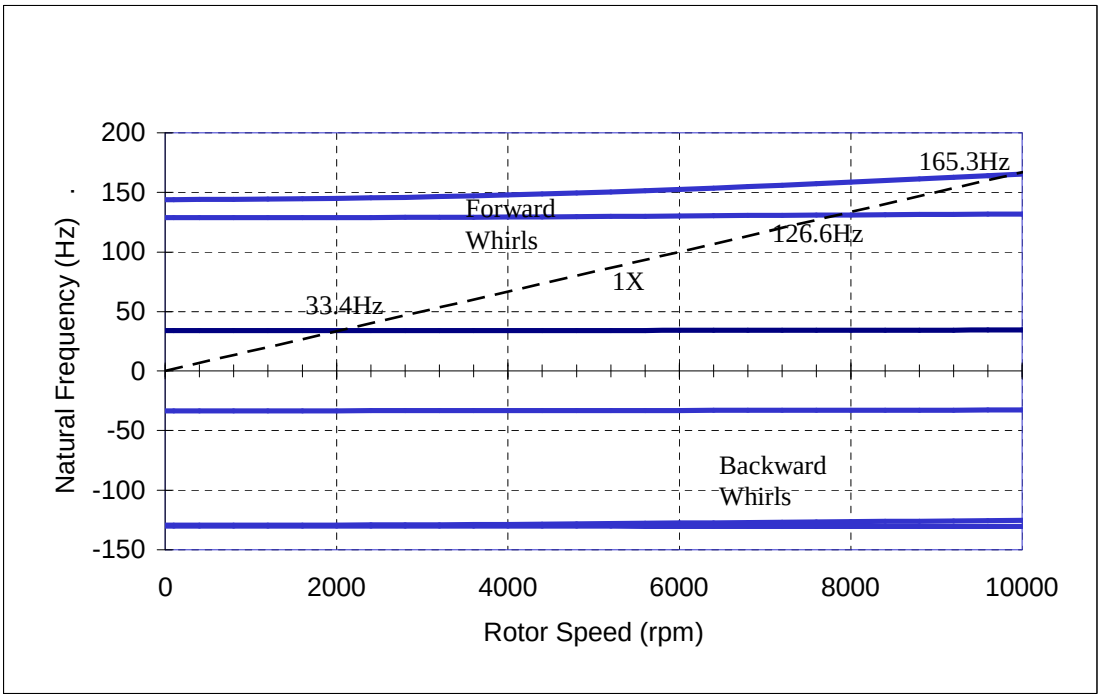

Figure 3.9 Campbell diagram for rotor.

The Campbell diagram is widely used for the prediction of occurrence of the resonances of the rotating system (see Figure 3.9). In the Campbell diagram, natural frequency is presented as a function of running speed. As the speed increases, gyroscopic effects cause a change in natural frequency, resulting in the bifurcation of forward and backward whirl. The synchronous (dashed) line has a slope of 1. The critical speed can be read at the intersection point of a unity slope line with the natural frequency line.

The natural frequencies of the rotor-bearing system determined on the Campbell diagram are 33.4Hz, 126.6Hz, and 165.3Hz. The value of the first critical speed was validated experimentally.

Also, critical speed of the system can be determined with another tool; i.e., undamped critical speed map. The undamped critical speed map shows the behavior of the critical speed as a function of the actual support stiffness. The critical speed can be read at the intersection point of the superimposed actual bearing stiffness line (175000 N/m) and frequency mode curves. The undamped lateral critical speeds map for the rotor-bearing system is shown in Figure 3.10.

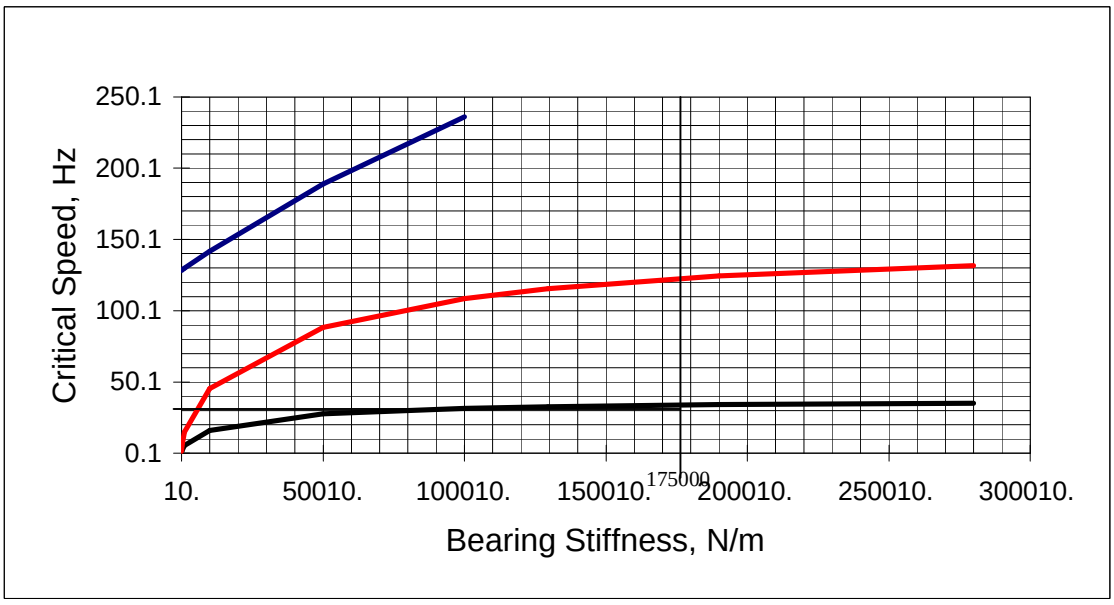

Figure 3.10. Undamped critical speed map.

The visualization of the mode shape at the first critical speed is shown in the Figure 3.12. The mode shape at the second critical speed is shown in Figure 3.13.

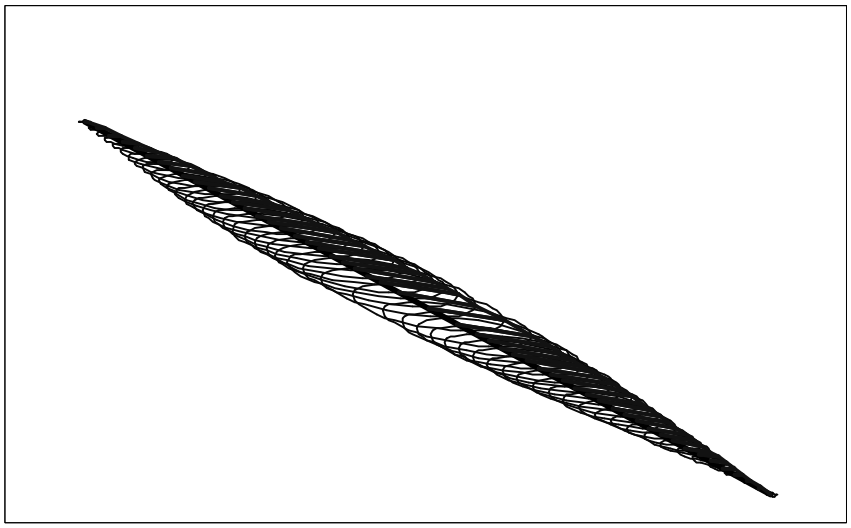

Figure 3.11 (a). First natural bending mode shape at 33.4 Hz (isometric view).

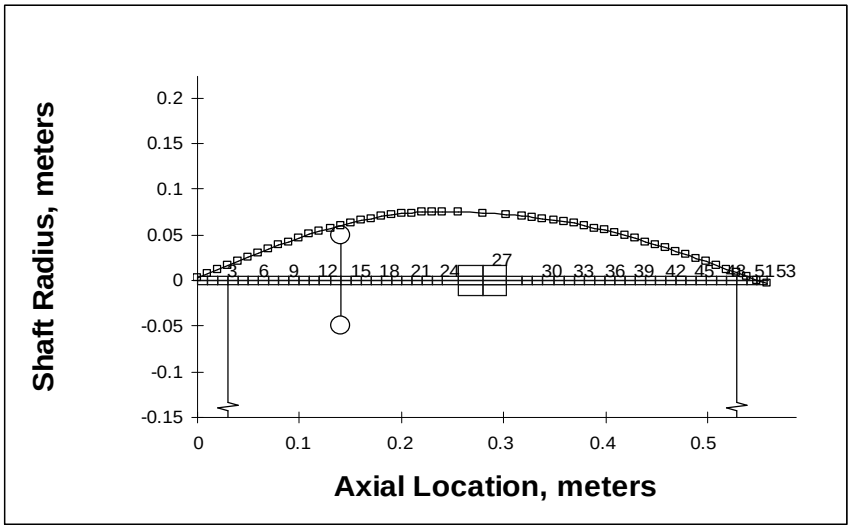

Figure 3.11 (b). **First natural mode shape at 33.4 Hz.**

In Figure 3.11(a, b), we can observe the first natural bending mode shape. The biggest deflection is on the midspan of the shaft.

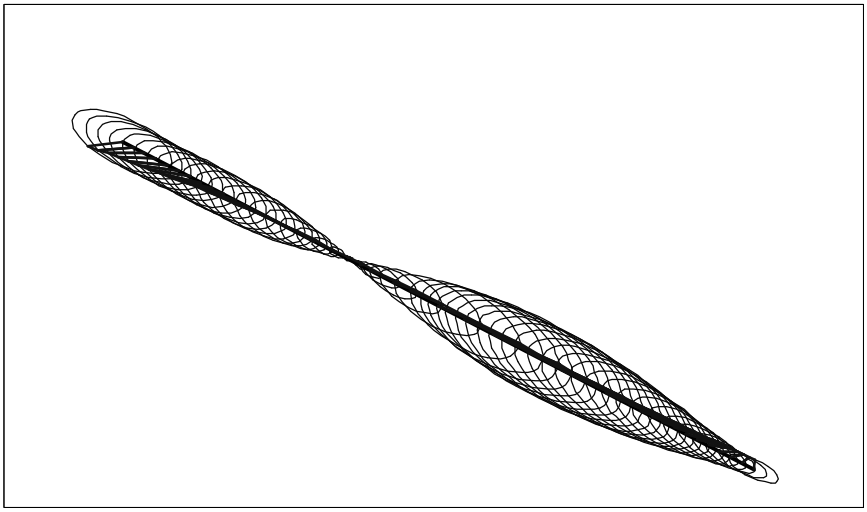

Figure 3.12 (a). **Second natural mode shape at 126.6 Hz (isometric view)**

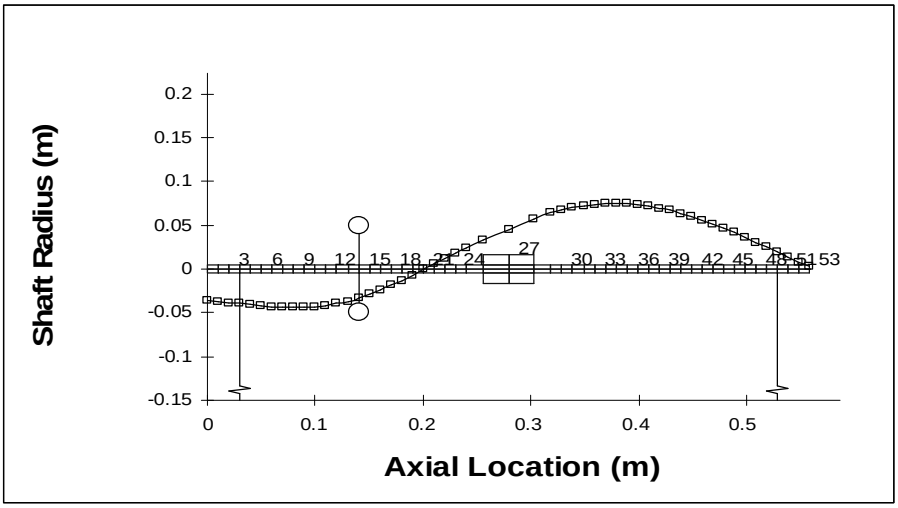

Figure 3.12 (b). **Second natural mode shape at 126.6 Hz**

For determining the magnitude of the unbalance of the system, a rotordynamics response analysis was performed. The finite analysis method was also used. Unbalance was located at the 15th node that matches to the point of the location of the balancing disc at the experimental rig. To obtain the same response as the real rotor response at measured nodes, the amount of 1.68 gm-in was placed at the 15th node. The response of the station no 27 that matches to the point of the location of the rotor of the active

magnetic actuator is shown in Figure 3.13. The response of the modeled node at the real rig was measured by the active magnetic actuator sensors and will be shown in Chapter IV.

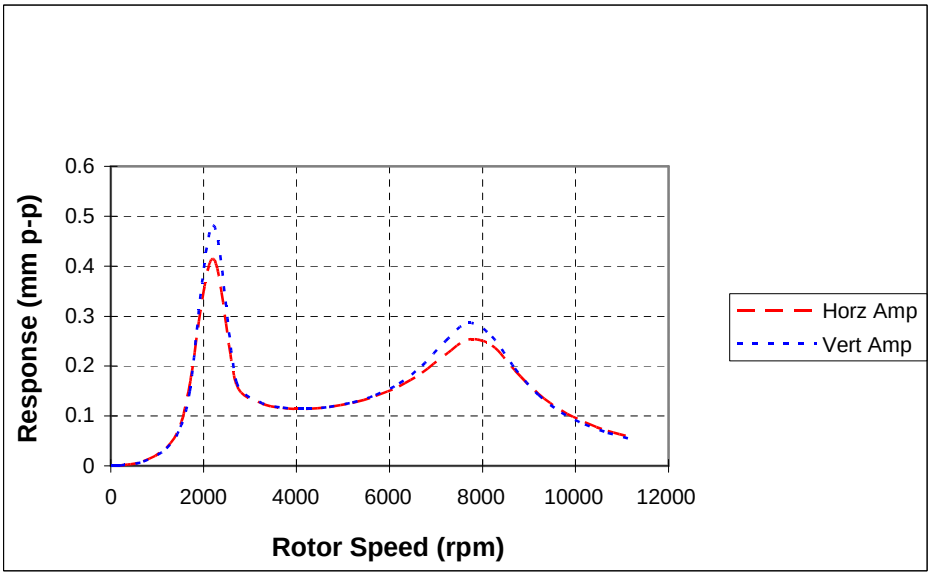

Figure 3.13. Simulated rotordynamics response plot at the location of the rotor of the active magnetic actuator.

The response of the 11th and 12th stations that matches the points of the location of the proximity probes is shown in Figures 3.14 and 3.15.

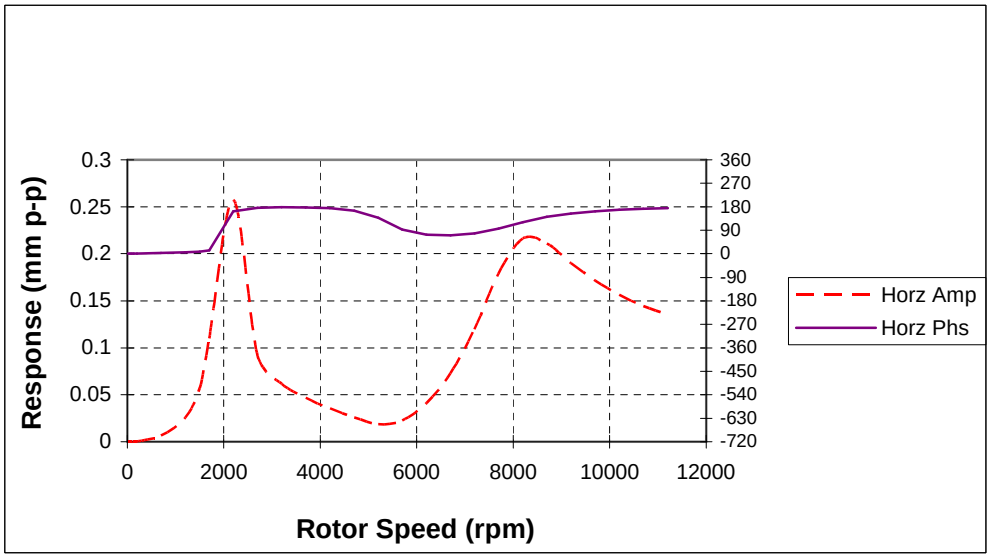

Figure 3.14. Simulated rotordynamic response plot at the location of the ADRE horizontal proximity probe.

In Figure 3.15, we can see response of the rotor modeled by the finite element method. In this plot, the modeled response of the 11th station on real rig is the location of the horizontal proximity probe. We can observe that the first resonant response occurs at the speed above 2,000 rpm with the amplitude 0.26 mm p-p that agreed well with real response plot created by ADRE with experimental data.

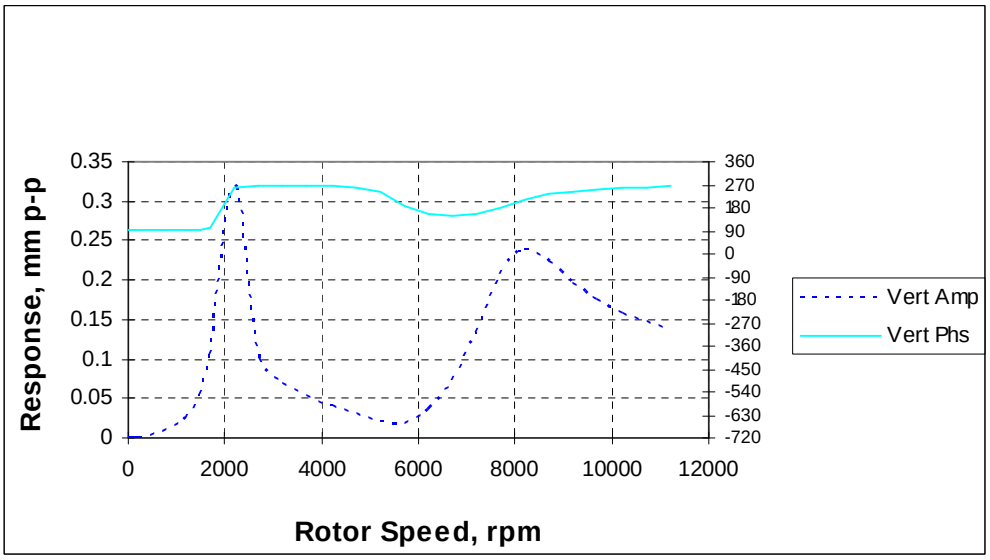

Figure 3.15. Simulated Rotordynamic Response Plot at the location of the vertical ADRE proximity probe.

From the analysis, one can validate the assumption that the system behaves like a Jeffcott rotor. Also, some parameters of the system were verified experimentally.

CHAPTER IV

UNBALANCE COMPENSATION EXPERIMENTAL RESULTS

4.1. Introduction

As previously stated an experiment was conducted on the rig with the following configuration. The shaft is 560 mm long (22 in), 10 mm (0.394 in) in diameter and supported by journal bearings. The active magnetic actuator is installed at the midspan of the shaft and one steel balance disk, 76.2 mm (3in) in diameter, 25.4 mm (1in) thick and 0.8kg (1.764lb) is attached at approximately one quarter of the shaft's span from the coupling. Two Wavetek sweep/function generators are used for generating and injecting sine wave current in the vertical and horizontal axis of the active magnetic actuator. The function generators are triggered with a once per revolution keyphasor. To determine the model identification, an impact hammer test was carried out. Two types of results are

presented in this work: one for constant subcritical speed and the second for speed range crossing the resonant first natural frequency.

4.2. Experimental Results.

4.2.1. System Identification.

The model validation of the experimental rig was performed for the configuration described above with the active magnetic actuator turned “off” (no injection). The transfer function of the rotor was measured using impact hammer modal testing. The measurements were carried out on the non-rotating rotor in the vertical plane. The calibrated impulse hammer excited the rotor at the non-drive end. The response of the rotor was measured with an accelerometer, fixed on the rotor. The input and output were analyzed using the Hewlett Packard 35670A dynamic signal analyzer shown in Figure 4.1.

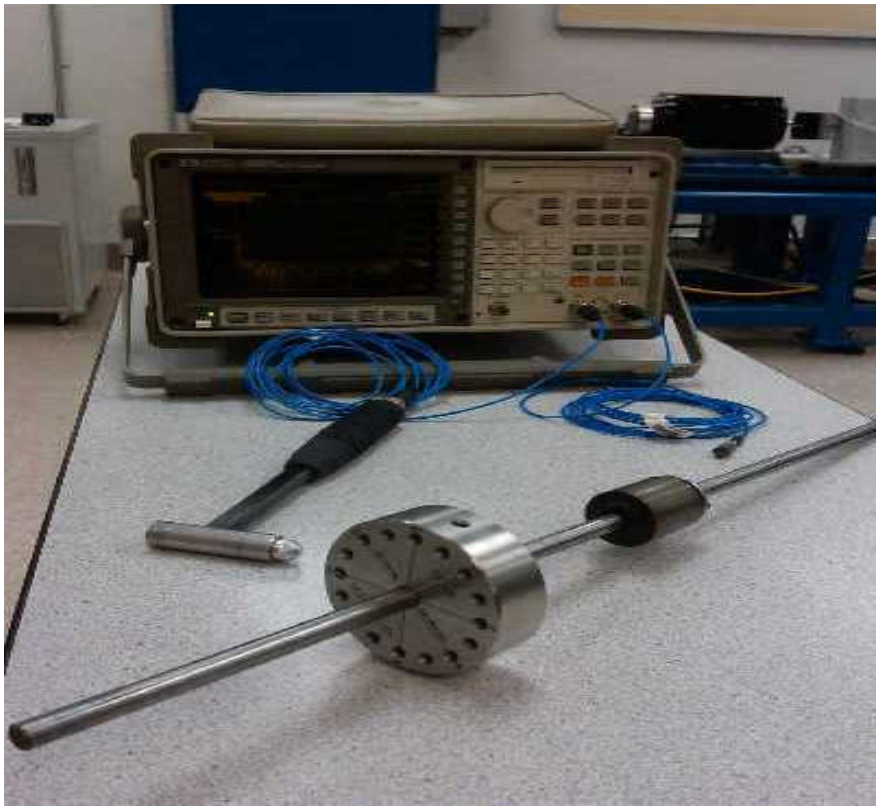

Figure 4.1 Hewlett Packard 35670A dynamic signal analyzer, impulse hummer, accelerometer and assembled rotor removed from bearings.

Figure 4.2 shows the resulting transfer function of the experimental rig. The data coincides very well with the prediction obtained by finite element modelling.

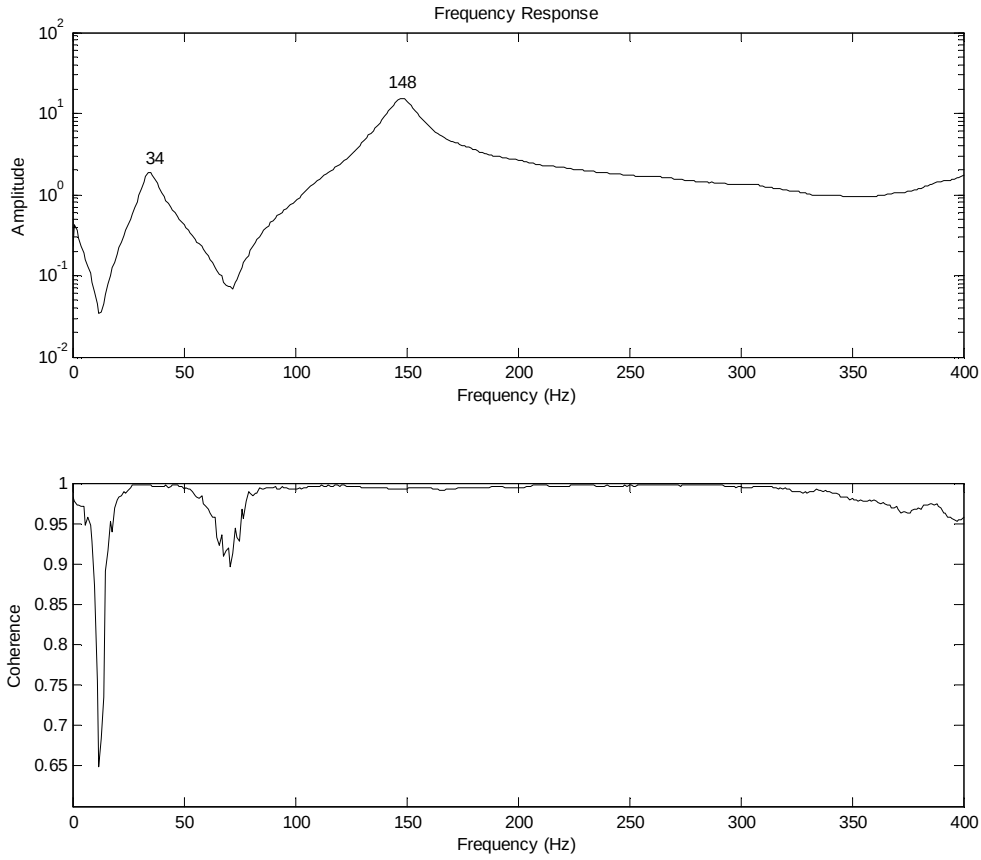

Figure 4.2 Transfer function of the experimental .

4.2.2 Constant Speed

For the first set of experiment, a subcritical speed of 1,950 rpm (32.5 Hz) was chosen and vibration measurements were collected. Then, an injection of current of the type discussed in Chapter III was applied to the magnetic actuator. Vibration measurements were again collected. Figure 4.3 shows the position of the response lines of the shaft in the vertical and horizontal vibrations. Note that the position responses are 90^0 out of phase. Also in this figure, it is shown that generated current will later be injected in the

vertical and horizontal direction to decrease the position response amplitudes. Amplitudes of the vertical and horizontal injections are 0.69 A and 0.66 A, respectively. The frequency is the same for all of the lines and corresponds to the rotating speed of 1,950 rpm (32.5 Hz).

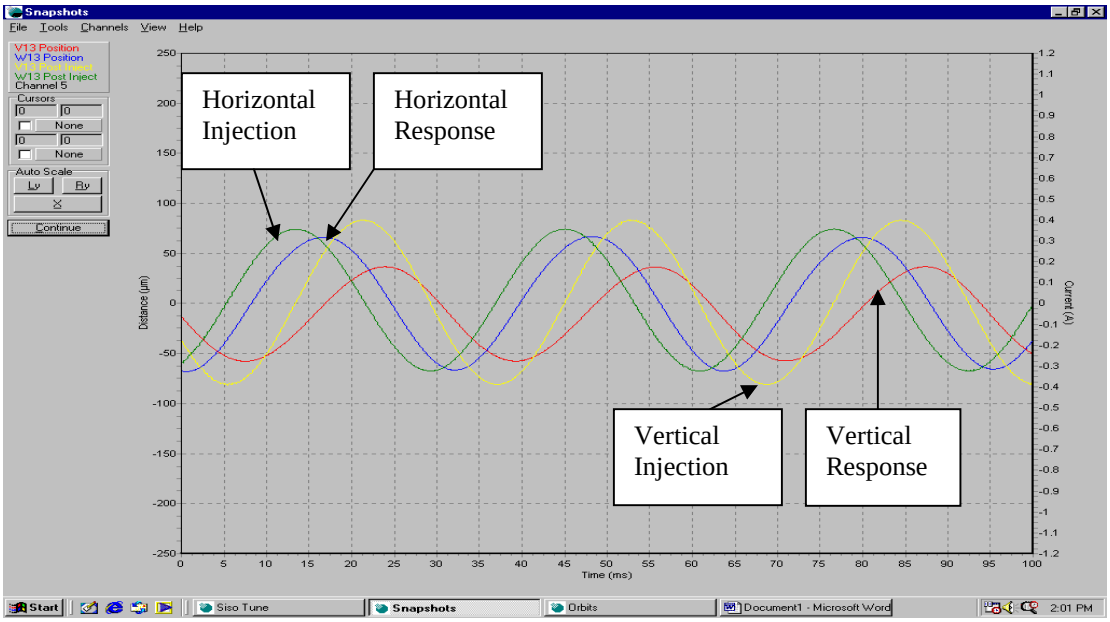

Figure 4.3. Uncompensated response of the shaft at magnetic actuator sensor and required current.

In Figures 4.3 through 4.7, the V13 and W13 positions represent the response of the shaft in the vertical and horizontal planes respectively. The V13 Post Inject and W13 Post Inject represent the current injected into the active magnetic actuator's poles in the vertical and horizontal axes, respectively.

Figure 4.4 presents the statistical information of the uncompensated response and generated current.

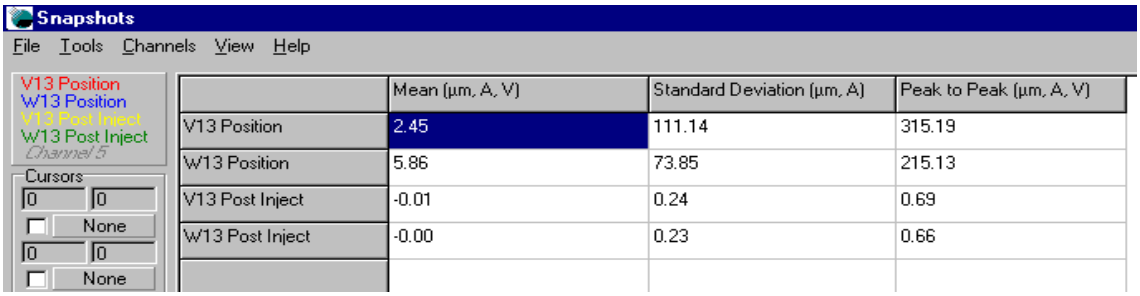

	Mean (µm, A, V)	Standard Deviation (µm, A)	Peak to Peak (µm, A, V)
V13 Position	2.45	111.14	315.19
W13 Position	5.86	73.85	215.13
V13 Post Inject	-0.01	0.24	0.69
W13 Post Inject	-0.00	0.23	0.66

Figure 4.4 Statistical data of the uncompensated response and required current.

Note that the vertical sensors in the magnetic actuator are labeled V13 and the horizontal sensors of the magnetic actuator are labeled W13. Also, note that due to the modification of the actuator, the vertical axis is actually opposite in signs to the data shown.

Figure 4.5 shows the orbit of the shaft measured by the proximity probes that are located next to the balance disk (corresponding to the 12th and 11th element at the finite element model).

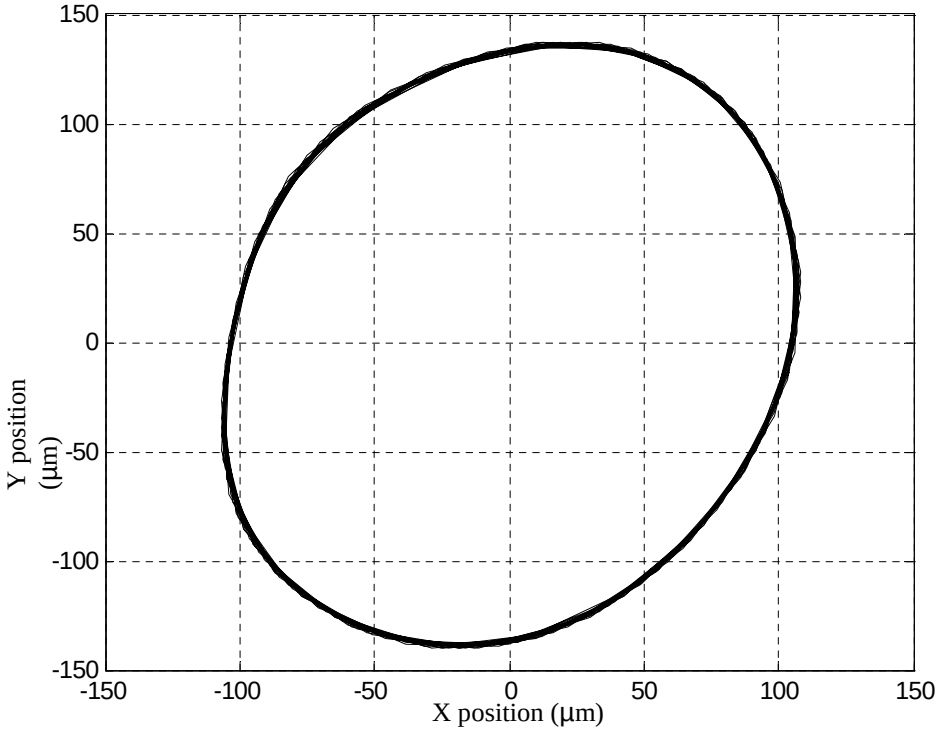

Figure 4.5 Orbit of the shaft without injection.

Figure 4.6 shows the response of the shaft and injected current in the vertical and horizontal directions. Data was measured by the sensors on the active magnetic actuator.

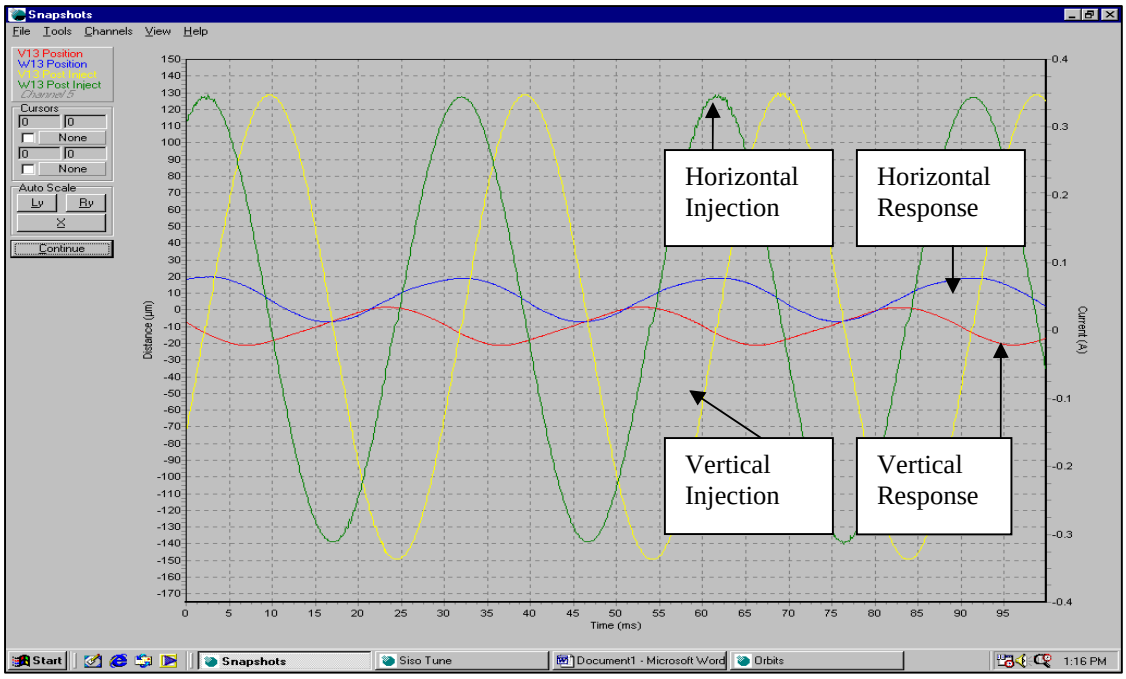

Figure 4.6 Response of the shaft after compensation and injected current.

The statistical evaluation of the results for the vertical and horizontal response and injected current are presented in Figure 4.7. This data was also obtained from the active magnetic actuator's sensor rings.

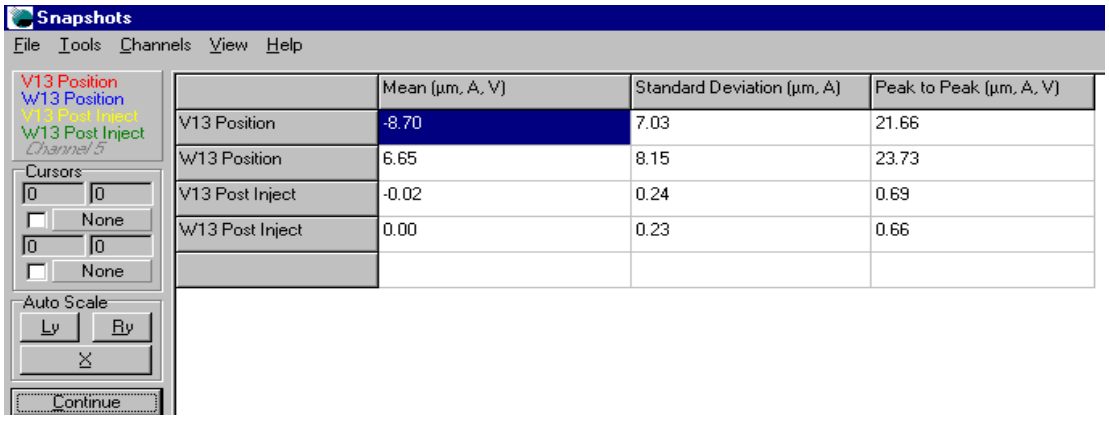

	Mean (µm, A, V)	Standard Deviation (µm, A)	Peak to Peak (µm, A, V)
V13 Position	-8.70	7.03	21.66
W13 Position	6.65	8.15	23.73
V13 Post Inject	-0.02	0.24	0.69
W13 Post Inject	0.00	0.23	0.66

Figure 4.7 Statistical data of the compensated response of the shaft and injected current.

The response of the rotor was also measured by the ADRE proximity probes. ADRE data, presented in Figure 4.8, shows the orbit of the shaft measured at the position next to the balance disk, after the force was applied to the shaft by the magnetic actuator.

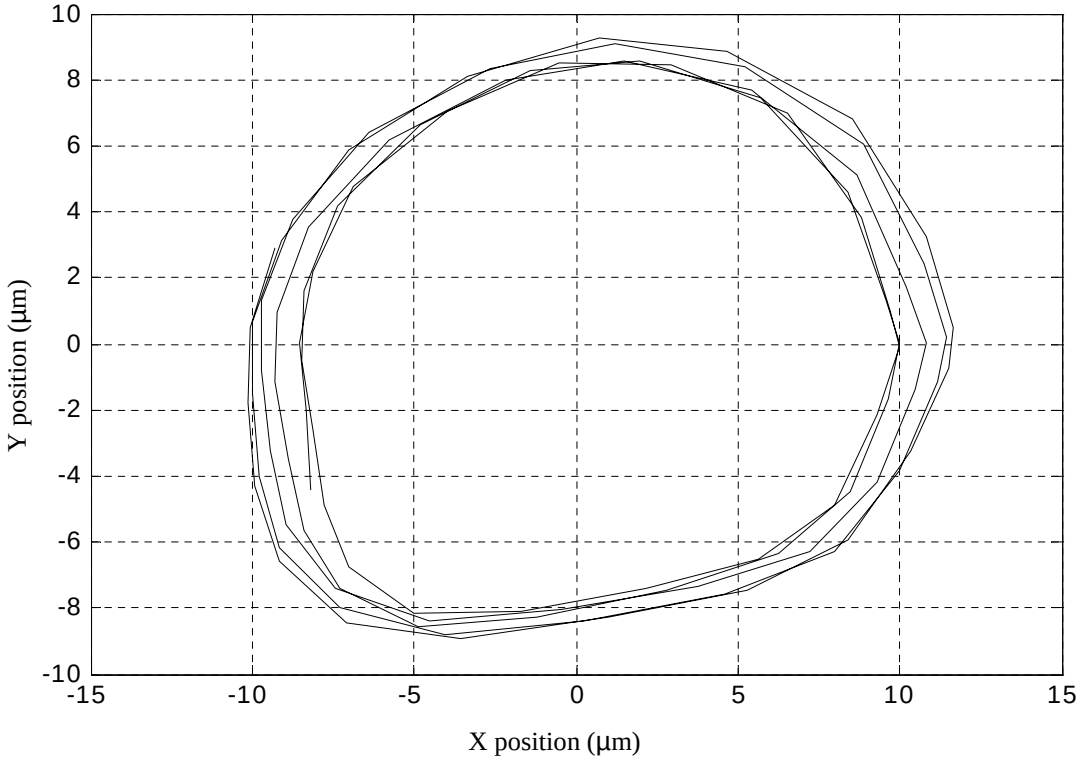

Figure 4.8 Orbit of the shaft with injection.

In Figures 4.6 through 4.8, a significant reduction in the vibration amplitude of the shaft is observed. Figure 4.9 compares the vibration amplitude both with and without current injection on the same scale. A reduction of amplitude of over 90% was achieved.

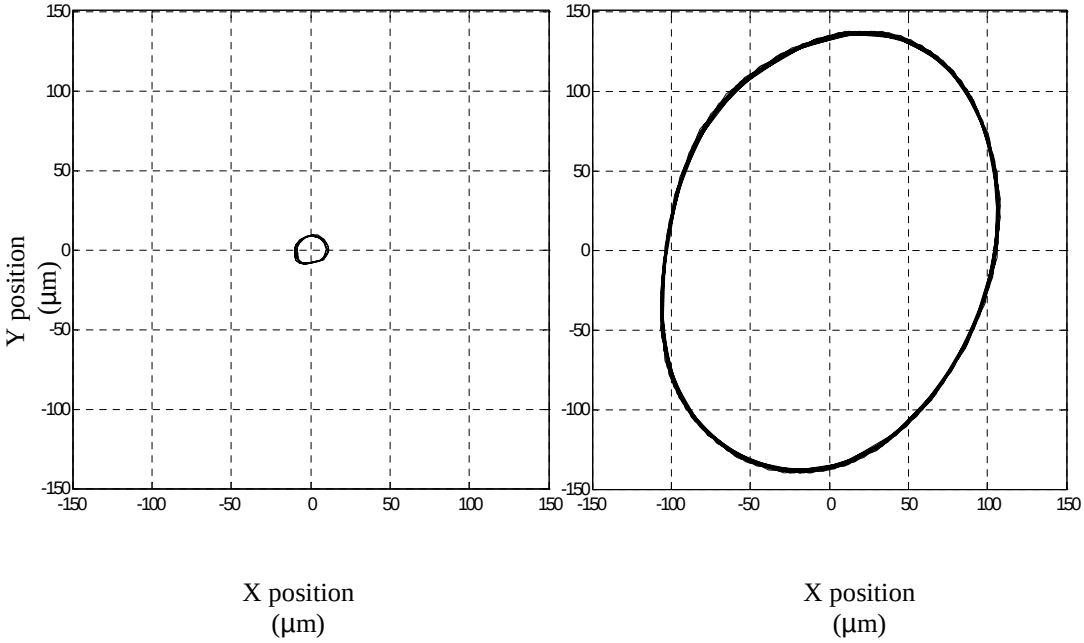

Figure 4.9 (a, b). Orbit of the shaft(a) with current injection, b) without current injection.

In Figure 4.8, we can observe the reduction of the vibration by more than 90%. The shaft was rotated at a constant subcritical speed of 1,950 rpm (32.5 Hz), than from a wave generator triggered by the Keyphasor sine shape current wave was sent to the active magnetic actuator. The amplitude of the current wave was 0.69A peak-to-peak and the frequency was the same as the rotation of speed 32.5 Hz.

4.2.3 Speed Ramp

The speed range experiment was conducted where the rig speed was ramped up through resonance and constant frequency injection, which was used to control vibrations passing through the critical speed. Figures 4.9 through 4.11 show the results of the speed ramp experiment.

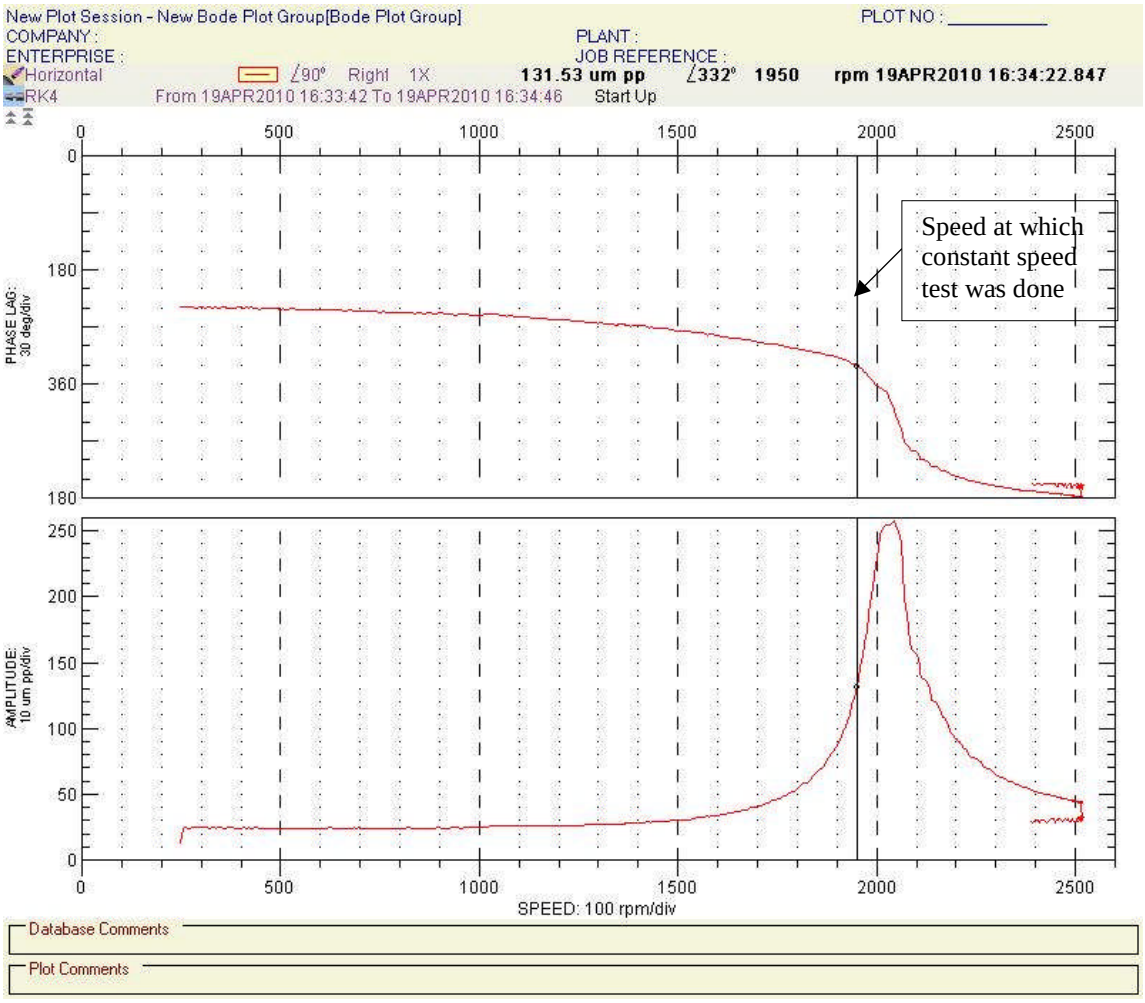

Figure 4.10. Experimental Bode plot (no injection).

Figure 4.9 shows the experimental Bode plot, generated by the ADRE system. This Bode plot shows the rotor vibration response (magnitude and phase) as the rotor speed is increased from 250 rpm to 2,500 rpm. Resonance occurs at 2020 rpm with an amplitude 260 μm. Vibrations are measured by the proximity probes near the disk and processed by ADRE.

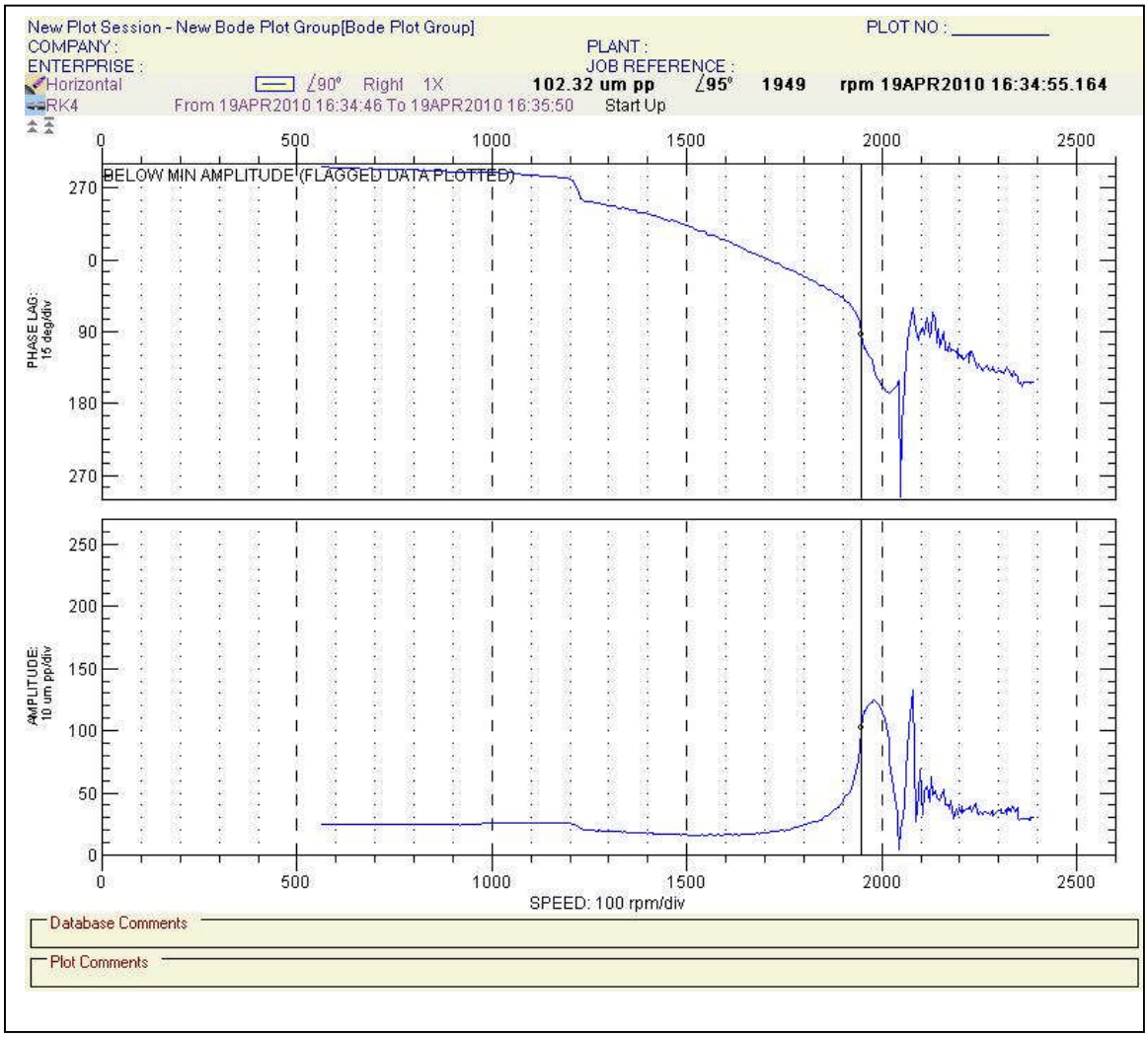

Figure 4.11. Experimental Bode plot of the rotor with injected current.

The response of the rotor with an injected force is shown in Figure 4.10. The experiment was conducted at a speed range up to 2,400 rpm. A wavetek signal generator was triggered by the Keyphasor and generated a sinusoidal signal with a frequency of 33.7 Hz. We can see a 50% reduction in magnitude of the resonant response. For a better observation, Figure 4.11 shows the response of the rotor with and without an injected force presented on the same plot.

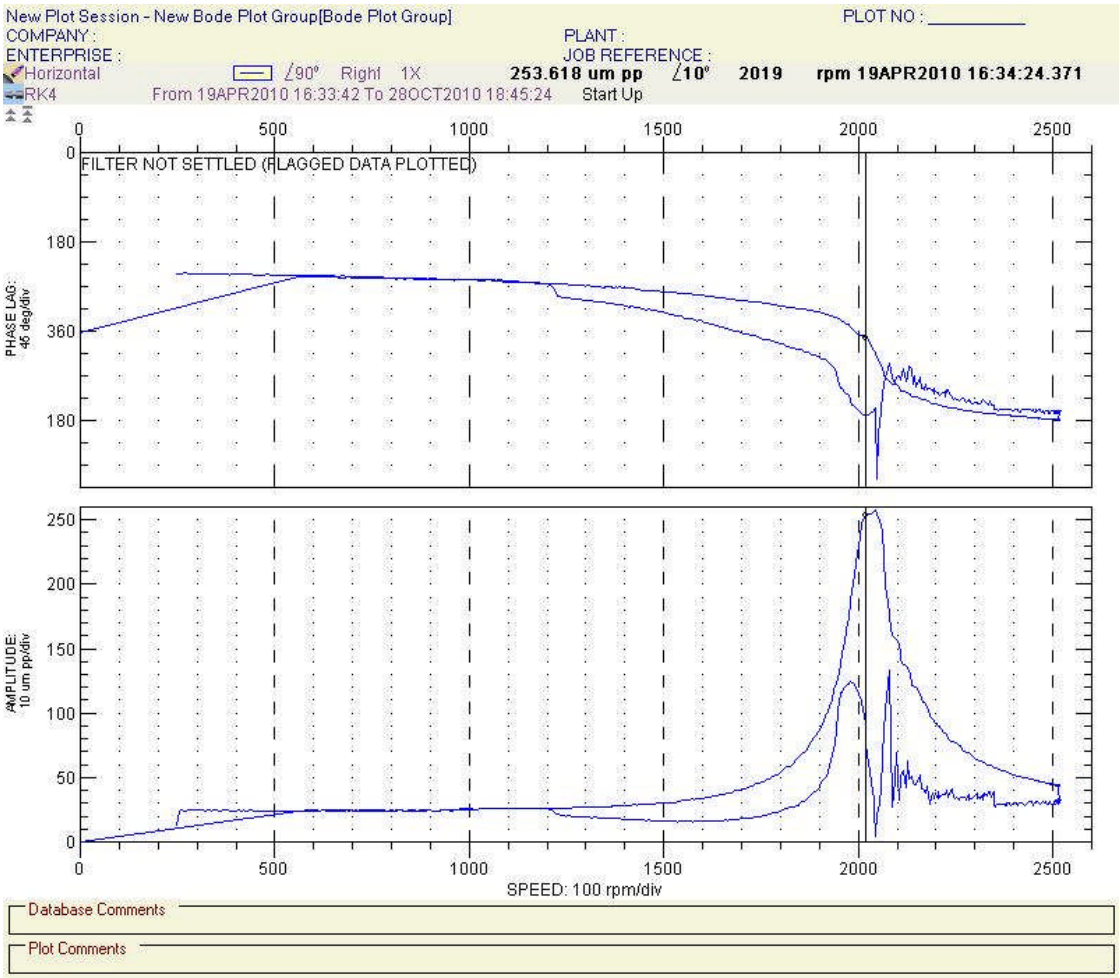

Figure 4.12. Response of the rotor over the speed range with and without current injection.

Due to limitations of the equipment, it is not possible to adjust the frequency of the injected generated signal in real time. At all speeds in the range of the experiment, the generator produced a constant frequency wave for every revolution of the shaft. A better result could probably be achieved if the generator could change the injection frequency according to the rotational speed.

CHAPTER V

CONCLUSIONS

5.1 Summary

A novel method for vibration control of a flexible rotor using a feed-forward signal and magnetic force actuator has been studied. The method was discussed and an analytical solution of the required magnetic actuator current, to cancel the steady state vibrations, was found. An experimental was discussed, including the generation of a system transfer function using a finite element method and rotordynamics modeling of the rig. A Campbell diagram, critical speed map, unbalance response simulation, and mode shape analysis were done. The flexible rotor model was confirmed by the impulse hammer modal testing method. The proper current was modified to be applicable for readily available signal generator hardware and demonstrated to be effective using numerical simulations. The vibration control method was confirmed by operating the at a constant speed and at changing speeds and comparing its behavior with and without the

control method applied. An approximately 90% reduction in vibration amplitude was achieved.

5.2 Contributions

The new method was proposed for the control of vibrations for a flexible rotor. The method uses a magnetic actuator and feed-forward of single frequency harmonic current signals which counteract the unbalance force. It is unique because of the simplistic application of the harmonic control signal, but it maintains the practical effectiveness of more complicated approaches. Because of this, the proposed method is more useful to industry than the current methods, which require specialized hardware.

5.3 Future Research Directions

This work can be further developed in a few areas. Studies could be conducted to examine the influence of the change of location of the actuator on the effectiveness of the vibration control. For example, the actuator can be located at the main unbalance location for the maximum effect, located near the bearing for minimum interference of the machine function, or at other locations to control other modes of vibration. Also, this method could be studied in a real world application by using an actual machine with realistic unbalance issues as a . An important area of improvement is the creation of an automated algorithm for injection tuning. This will speed the process and may be able to achieve slightly greater levels of vibration cancelling.

Some problems have been analyzed in this work, and the results may now be summarized. The following conclusions emerge.

A new method for the control of flexible rotor system vibration using an active magnetic actuator was established. Going to this goal theoretical explanation of the remodeled rotor was reviewed. This review lead to the more precise formula for force and required current calculations.

The finite element model of the rig was developed. The modeling produced results indicative of the actual rotor dynamic behavior.

REFERENCE

1. Alauze, C., Der Hagopian, J., Gaudiller, L., Voinis Ph., "Active Balancing of Turbomachinery: Application to Large Shaft Lines," *Journal of Vibration and Control*, volume 7 no.2 p-p. 249-278, 2001

2. Burrows, C.R., Sahinkaya, N., Traxler, A., Schweitzer, G., "Design and Application of a Magnetic Bearing for Vibration Control and Stabilization of a Flexible Rotor," *Proceeding of the First International Symposium on Magnetic Bearings*, Zurich, June 6-8, 1988

3. Czolczynski, K., *Rotordynamics of Gas-Lubricated Journal Bearing System*, Springer-Verlag, New York, Inc. 1999

4. Dimentberg, F.M., *Flexural Vibration of rotating shafts*, Butterworths', London. 1961

5. Earnshaw, S., "On the Nature of the Molecular Forces witch Regulate the Constitution of the Lumiferous Ether," *Trans. Of the Cambridge Philosophical Society*, Vol. 7, Part I, pp. 97-112. 1842

6. Ehrich, F., *Handbook of Rotordynamics*, McGRAW-HILL, Inc., New York. 1992

7. Findeisen, D., *System Dynamics and Mechanical Vibrations*, Springer-Verlag, New York. 2000

8. Foppl, A., "The shaft of the Laval Steam-Turbine," *Der Civilingenieur pp.332-342* 1895

9. Genta, G., *Vibration of structures and machines*, Springer-Verlag. New York. 591p. 1999

10. Habermann, H., Liard, G., "Practical Magnetic Bearings," *IEEE Spectrum,* Vol. 16, No. 9. September 1979

11. Jeffcott, H., "The lateral vibration of loaded shafts in the neighborhood of a whirling speed-the effect of want of balance," *Phil. Mag.,* volume 37, no. 6, pp. 304-314. 1919

12. Kapitsa, P.L., "Ustoichivost I perekhod cherez kriticheskie oboroty bistro vraschayschihsja rotorov pri nalichii treniya," *Zurnal teknicheskoi fiziki, IX,* Vypusk 2, 1939

13. Kasarda, M.E.F., Mendoza, H., Kirk, R.G., Wicks, A., "Reduction of subsynchronous vibrations in a single-disk rotor using an active magnetic damper," *Mechanics Research Communications*, volume 31, issue 6, pp. 689–695, 2004

14. Knospe C.R., Hope, R.W., Tamer, S.M., Fedigan, S.J., **"**Robustness of Adaptive Unbalance Control of Rotors with Magnetic Bearings," *Journal of Vibration and Control*, volume. 2, no. 1, pp. 33-52, January 1996

15. Kramer, E., *Dynamics of Rotors and Foundations*, Springer-Verlag, New York, 1993

16. Krodkiewski, J.M., Sun, L., "Self-Tuning Adaptive Control of Forced Vibration in Rotor Systems Using an Active Journal Bearing," *Journal of Sound and Vibration*, volume 231, pp. 1-14. 1998

17. Kai-Yew, L., Coppola, V. T., Bernstein, D. S., "Adaptive Auto centering Control for an Active Magnetic Bearing Supporting a Rotor with Unknown Mass Imbalance," *IEEE Transactions on control systems technology*, volume 4, no 5, September 1996

18. Muszynska, A., "Fundamental Response of a Rotor," *Bently Rotor Dynamic Research Corporation*, Minden, NV. 1986

19. Natanzon, V. Ya., "Frequencies of flexular vibration of a rotating shaft," *Transactions of the Institute "Oborongiz"*, no 142, 1948

20. Nelson, F.C., "Rotor Dynamic without Equations," *International Journal of COMADEM*, volume 10, no3, pp. 2 – 10, July 2007

21. Nikolai, E.L, "K teorii gibkogo vala," *Trud. Leningrad Ind. Inst., Razdelenie Fiziki-Matematicheskikh Nauk*, vypusk 3, no 6, 1937

22. Querioz, De M.S., "An Active Identification Method of Rotor Unbalance Parameters," *Journal of Vibration and Control*, volume 15, no 9, 2009

23. Rankine W. J. Mc. Q, "Centrifugal whirling of shafts," *The Engineer (London)*, volume 26, April 8, p.249, 1869

24. Rayleigh, J. W., *The theory of sound Volume 1*, MacMillan, 2nd revised edition, Cambridge, 1894

25. Sawicki, J. T., Fleming, D. P., Poplawski, J.V., "Unbalance Response Prediction for Accelerating Rotors with Load-Dependent Nonlinear Bearing Stiffness," *Third Biennial International Symposium on Stability Control of Rotating Machinery (ISCORMA-3),* 2005

26. Schweitzer, G., "Characteristics of a Magnetic Rotor Bearing for Active Vibration Control," *First International Conference on Vibrations in Rotating Machinery*, 1976

27. Sun, J.C., Wang, X.G., Xi, F.J., "Sliding mode active vibration control of circular saws," *International Conference on Control Applications, IEEE,* pp. 953-958, 2000

28. Tammi, K., "Active Vibration Control of Rotor in Desktop Test Environment," *Espoo VTT Publications 498,* pp. 82-176, 2003

29. Timoshenko, S. P., "On the correction factor for shear of the differential equation for transverse vibrations of bars of uniform cross-section," *Philosophical Magazine*, p. 744, 1921

30. Ulbrich, H., *Elements of Active Vibration Control for Rotating Machinery*, NASA Lewis Research Center, Cleveland, Ohio, May 1990

31. Vance, J. M., Rotordynamic of Turbomachinery, *John Wiley & Sons*, New York, 1988

32. Yu, H-C, Lin, Y-H, Chu, C-L., “Robust modal vibration suppression of a flexible rotor,” *Mechanical Systems and Signal Processing*, volume 21, pp. 334–347, 2007

Appendix A

Selected ADRE Data Acquisition in Horizontal Direction

Without Injection				With Injection			
Speed (RPM)	Average Amplitude (µm)	Average synchronous Amplitude (µm)	Average Phase (degrees)	**Speed (RPM)**	Average Amplitude (µm)	Average synchronous Amplitude (µm)	Average Phase (degrees)
1905	93.9	89.3	319	1905	48.27	47.05	52
1910	98.5	93	320	1910	50	48.64	54
1916	102	98.8	321	1917	51.6	50.4	56
1922	105	101	322	1922	54.7	53.8	59
1926	111	105	324	1934	71.7	66.8	66
1932	118	110	326	1939	84.4	76.5	73
1938	125	118	328	1945	84.4	85.1	79
1942	131	123	329	1949	107	102	95
1948	139	128	331	1955	115	115	111
1950	139	132	332	1958	115	115	111
1960	158	146	336	1960	120	117	113
1965	167	155	338	1968	123	122	123
1970	178	165	341	1975	123	123	126
1976	178	173	343	1980	128	124	136
1981	205	188	348	1985	128	124	145
1985	205	194	350	1990	128	122	150
1991	218	207	355	1996	125	118	156
1998	231	224	1	2001	125	115	158
2003	243	236	5	2008	120	110	162
2009	256	247	6	2013	116	103	165
2015	257	252	8	2017	104	92.3	167
2019	257	254	10	2020	94.8	75.5	168
2025	258	254	13	2040	59.4	32.26	157
2028	257	254	19	2042	59.4	25.33	155
2034	259	255	24	2045	24.28	4.755	1BMA
2040	261	257	35	2048	36.03	21.23	296
2044	264	258	38	2052	57.1	24.2	206
2045	264	258	40	2058	92.8	40.24	158
2046	264	258	42	2064	148	67.1	122
2060	262	246	66	2070	148	101	90
2062	262	242	69	2075	222	113	80
2069	192	199	92	2081	222	133	61
2076	192	186	96	2087	72.6	27.45	89
2082	161	166	101	2093	72.6	48.07	102
2086	156	160	104	2098	144	68.9	91

Speed (RPM)	Average Amplitude (µm)	Average synchronous Amplitude (µm)	Average Phase (degrees)	Speed (RPM)	Average Amplitude (µm)	Average synchronous Amplitude (µm)	Average Phase (degrees)
2093	153	158	105	2105	58.6	32.97	86
2100	153	156	107	2110	90.2	51.1	94
2107	146	148	114	2117	97.6	55.2	74
2110	139	141	118	2122	96.5	42.37	98
2114	135	138	119	2128	120	62.8	91
2122	134	137	120	2129	71.2	48.45	66
2130	133	133	123	2138	52.5	51.3	73
2134	129	131	124	2140	78.5	46.89	105
2139	119	121	128	2145	82.1	44.75	88
2146	119	120	129	2150	82.1	44.37	110
2152	118	119	130	2159	99.6	52.4	91
2162	110	111	135	2164	68.7	40.77	113
2166	107	108	136	2169	67.5	40.41	115
2171	105	107	136	2172	84.9	37.59	104
2176	105	105	138	2177	84.9	43.83	115
2181	103	103	139	2185	57.6	28.8	113
2184	96.2	98.3	141	2190	57.6	37.56	117
2189	96.2	96.8	142	2193	57.9	34.87	112
2195	93.4	94.5	143	2195	57.9	33.03	124
2198	91.9	92.6	144	2200	58	37.99	118
2202	91.9	92.1	144	2204	58	33.6	124
2207	89.5	90.1	145	2207	58.1	38.83	120
2210	89.5	89.5	146	2211	63.9	34.95	126
2212	88.8	88.3	147	2223	72.3	36.69	129
2216	86.2	86.2	148	2224	72.3	37.86	117
2220	83.9	85	148	2228	68.7	39.69	115
2223	83.9	84.2	149	2232	68.7	34.36	116
2227	84.9	83.8	149	2237	62.8	40.56	125
2232	80.6	80.6	151	2241	86.9	41.64	129
2232	80.6	80.6	151	2246	51.8	34.21	136
2239	78.9	78.4	152	2249	51.8	33.02	131
2242	77.8	77.8	152	2253	51.7	34.56	135
2244	77.8	77.6	152	2257	51.7	32.1	139
2249	76.8	76.8	153	2261	52.2	34.84	136
2254	76.4	76.1	154	2264	52.8	35.17	136
2259	76.4	75.3	154	2271	54.6	34.22	132
2263	74.1	74.3	155	2276	54.6	33.03	140
2265	74.1	73.1	155				
2270	72	70.8	157				
2272	70.6	70.6	157				

Appendix B

Finite element Analysis Input File

lumped mass (lbm)	length (in)	outer diameter (in)	inner diameter (in)	polar moment of inertia (lbm/in^2)	transverse moment of inertia (lbm/in^2)	modulus of elasticity ($PSI \times 10^6$)	Density (lbm/in^3)
0	1.18	0.39	0	0	0	25	0.30
0	2.07	0.39	0	0	0	25	0.30
0	2.07	0.39	0	0	0	25	0.30
1.76	2.07	0.39	0	2.05	1.14	25	0.30
0	2.07	0.39	0	0	0	25	0.30
0	0.61	0.39	0	0	0	25	0.30
0	0.94	0.39	0	0	0	25	0.30
0	0.94	0.39	0	0	0	25	0.30
0	0.61	0.39	0	0	0	25	0.30
0	2.07	0.39	0	0	0	25	0.30
0	2.07	0.39	0	0	0	25	0.30
0	2.07	0.39	0	0	0	25	0.30
0	2.07	0.39	0	0	0	25	0.30
0	1.18	0.39	0	0	0	25	0.30
0	0	0.39	0	0	0	25	0.30

Appendix C

Radial Magnetic Actuator Specifications.

Actuator Performance Specifications		**Imperial Units**	**Metric Units**
Static Load Capacity		12 lbf	53 N
Saturation Current		3.00 A	
Current Stiffness, Ki		8.5 lbf/amp	38 N/amp
Position Stiffness, Kx		8.24+02 lbf/in	144E+05 N/m
Actuator Geometry			
Number Of Poles Per Quadrant		2	
Stator Stack Length		0.500 in	12.700 mm
Stator OD		2.788 in	70.822 mm
Stator ID		1.380 in	35.052 mm
Rotor OD		1.336 in	33.9344 mm
Nominal Gap		0.022 in	0.5588 mm
Small Pole Wight		0.207 in	5.245 mm
Pole Height		0.496 in	12.587 mm
Pole Centerline Angle		22.5 deg	0.394 rads
Material Properties			
Material Grade	Stator	M-19, C-5, 0.044	0.3556 mm
	Rotor	Arnon 5, C-5, 0.005	0.127 mm
Saturation Flux Density		1.25	48.0 mic.ohm.cm
Relative Permeability		3000	0.07 N/cu.cm
Lamination Thickness:	Stator	0.014	733 C
	Rotor	0.005	
Coil Specifications			
Wire Gauge		23 AWG	1.923 mm
Wire type		Hyslik 200 heavy/round	
Coil Insulation		0 in	0 mm
Turns Per Coil		114	
Coil Extension (max)		0.316 in	8.0264 mm
Quadrant Resistance (calculated)		0.912 ohm	
Quadrant Inductance (nominal)		6.116 mH	
Power Amplifier Specifications			
Maximum Continuous Current		3 amp	
Peak Current		10 amp for 2 seconds	
Max DC Supply Voltage		48 V	
Minimum Required Voltage		38.67 V	
Minimum Load Inductance		250 micro-H	
Switching Frequency		20 kHz	
Position Sensor Specifications			
Type		Variable Reluctance	
Number per axis		1	